Evolutionarily conserved role of serotonin signaling in regulating actomyosin contractility during morphogenesis

Sanjay Karki[1], Mehdi Saadaoui[1], Valentin Dunsing[1], Elise Da Silva[1], Jean-Marc Philippe[1], Cédric Maurange[1], Thomas Lecuit[1,2,*]
[1]Aix-Marseille Université & CNRS, IBDM - UMR7288 & Turing Centre for Living Systems, Marseille, France
[2] Collège de France, Paris, France
[*] Lead Contact: thomas.lecuit@univ-amu.fr (T.L)

Serotonin is a neurotransmitter that signals through 5-HT receptors to control key functions in the nervous system. Serotonin receptors are also ubiquitously expressed in various organs and have been detected in embryos of different organisms. Potential morphogenetic functions of serotonin signaling have been proposed based on pharmacological studies but a mechanistic understanding is still lacking. Here, we uncover a role of serotonin signaling in axis extension of *Drosophila* embryos by regulating MyosinII (MyoII) activation, cell contractility and cell intercalation. We find that serotonin and serotonin receptors 5HT2A and 5HT2B form a signaling module that quantitatively regulates the amplitude of planar polarized MyoII contractility specified by Toll receptors and the GPCR Cirl. Remarkably, serotonin signaling also regulates actomyosin contractility at cell junctions, cellular flows and epiblast morphogenesis during chicken gastrulation. This phylogenetically conserved mechanical function of serotonin signaling in regulating actomyosin contractility and tissue flow reveals an ancestral role in morphogenesis of multicellular organisms.

The neurotransmitter serotonin is a monoamine produced by the decarboxylation of the amino acid tryptophan. It is evolutionarily conserved in protozoa and most metazoans studied (1,2,3,4,5,6,7) and is also present in plants (8,9). Serotonin functions via serotonin receptors, which are estimated to have evolved around 800 million years ago (reviewed in 10). Seven subtypes of serotonin receptors (5HT1-5HT7) have been identified in vertebrates (11); most of which are phylogenetically conserved across many species (12,13, reviewed in 14) including insects such as *Drosophila melanogaster* (fruit fly), *Tribolium castaneum* (beetle), *Aedes aegypti* (mosquito) (15). All the 5HT receptors except 5HT3R which is a gated ion channel receptor, are seven-pass transmembrane G protein-coupled receptors. Serotonin and G protein-coupled serotonin receptors have a wide range of functions in modulating physiological and behavioral processes in animals. In addition, the serotonergic system has non-neuronal functions such as energy balance, pulmonary, cardiac, gastrointestinal, and reproductive function (reviewed in 16).

The morphogenetic function of serotonin was first purposed and reported by Buznikov and colleagues in the 1960s, based on their studies on sea urchin embryos (reviewed in 1, 7), where inhibition of serotonin signaling leads to the blockage of extension of the archenteron, the embryonic primitive digestive tube. Subsequent work in sea urchin (17,18), chicken (19, 20, 21), *Xenopus* (21,22,23,24,25), mouse (26) and *Drosophila* (27,28,29) reported the potential role of serotonin in activating intracellular contractile elements that drive morphogenetic cell movements. In the chicken, serotonin has been detected in the embryo during primitive streak formation (21). Morphological defects have been characterized during embryogenesis following the pharmacological treatments targeting the serotonin receptors (19,20,21), however the link to the morphogenetic processes/mechanisms, which were not understood at the time, was lacking.

Large-scale directed tissue-flow is observed during morphogenesis in many organisms. For example, during the primitive streak formation in chicken embryos and axis extension (germ-band extension) in *Drosophila* (reviewed in 35). Cell intercalation by polarized remodeling of the cell-cell contacts via actomyosin contractility drives tissue extension. Apical cell-cell contacts contract along the midline and then extend along the anterior-posterior axis resulting in tissue convergence and extension along these axes (30, 31, 32, 33, 34 and reviewed in 35). In *Drosophila*, polarized actomyosin contractility drives the polarized junctional remodeling and hence the polarized cell rearrangements (31, 32). Toll receptors (Toll 2, 6 and 8) are required for the planar polarization of MyoII junctional recruitment (36, 37). A recent study showed that the Toll-8 and the adhesion GPCR Cirl/Latrophilin interact and self-organize to form a polarizing field to facilitate asymmetric activation of MyoII at the cell-cell interface (37). There is increasing evidence that GPCR signaling instructs the activation of actomyosin contractility in many morphogenetic processes (37,38,39,40,41 and reviewed in 35 and 42). In particular, *Drosophila* has 5 genes coding for GPCR serotonin receptors: 5HT1A, 5HT1B, 5HT2A, 5HT2B, and 5HT7 (43,44). Serotonin has been detected at its peak level at the onset of axis extension (45). However, the function of serotonin and serotonin receptors during axis extension, which is driven by actomyosin contractility (31,32), remains elusive. Serotonin and GPCRs serotonin receptors have been identified in embryos of many organisms, including *Drosophila* (27) as described above, but whether they are involved in the regulation of actomyosin contractility has never been investigated.

In this study, we used invertebrate (*Drosophila*) and vertebrate (chicken) embryo model systems to investigate the potentially evolutionarily conserved role of serotonin and GPCR serotonin receptors during axis extension and regulation of cellular mechanics.

Results

5HT2A is required for tissue flow, cell intercalation and MyoII activation in the *Drosophila* ectoderm

The *Drosophila* ectodermal tissue is on the lateral side of the embryo and undergoes convergence (along the Dorsal-Ventral; DV axis) and extension (along the Anterior-Posterior; AP axis) as the posterior pole of the embryo invaginates and moves towards the anterior (46,47) (Fig. 1a). We first asked whether 5HT2A is required for *Drosophila* axis extension using a null mutant based on homologous recombination (hereafter *5HT2A -/-*) (43,44). In a previous study (29), germ-band extension defects were reported in a non-specific deficiency line which covers another gene. Here, we re-examined this issue using a specific null mutant (*5HT2A-/-)* and analyzed the phenotypes at the tissue and cellular level. To determine whether 5HT2A mutation affects axis extension at the tissue level, we followed the progression of the posterior midgut in differential interference contrast (DIC) videos (Extended Data Fig. 1a-b and Video 1). We observed a 10-12 min delay in axis extension in maternal and zygotic *5HT2A* mutant embryos compared to wild-type embryos (Extended Data Fig. 1a-b and Video 1). Consistently, local tissue extension, as measured by tracking the centroid distance between two cells was significantly reduced (Extended Data Fig. 2a,b). Tissue extension is driven by cell intercalation which happens through T1 transition (31) and rosettes formation (48). We tracked T1 events and found marked reduction (Fig. 1b,c) whereas rosettes formation was not significantly affected (data not shown). Cell intercalation is coordinated by spatiotemporal pattern of actomyosin contractility (49,50). The planar polarized activity of MyoII at the junctions (MyoII is enriched in the vertical junctions) (31) and the planar polarized flow of the medial-apical MyoII (32) power polarized junctional remodelling (46) during cell intercalation. We next investigated the temporal evolution of MyoII distribution every 5 minutes, starting 30 minutes

after the cellularization front passes the nucleus or 20 minutes before dorsolateral cell division. This time corresponds to the transition of the tissue movement towards the posterior. We observed an overall reduction of the junctional (Fig. 1d, Extended Data Fig. 2c and Video 2) and medial MyoII levels (Fig. 1d,g and Video 2) at all the time points. We examined the MyoII levels in DV oriented and AP oriented junctions, which allowed us to quantify the amplitude of polarity. MyoII levels at both categories of junctions were significantly reduced at all time points (Fig. 1e), however the amplitude of polarity, was reduced only initially (Fig. 1f). Medial-apical MyoII promotes E-cadherin clustering (51). We observed reduced levels and polarity of E-cadherin (Extended Data Fig. 2e-g and Video 2), consistent with the reduction in medial MyoII levels. Taken together, 5HT2A recruits both junctional and medial MyoII and alters E-cadherin levels. To confirm the phenotype of 5HT2A mutation, we next studied gain of 5HT2A function by overexpressing the wild-type 5HT2A receptors. Assuming that G-proteins and downstream effectors are abundant, over-expression of 5HT2A would be expected to increase both junctional and medial MyoII levels. Consistently, we observed an increase in the junctional MyoII levels (Fig. 1h, Extended Data Fig. 2d and Video 3). However, the medial MyoII levels did not increase (Fig. 1h,k). On closer inspection, we found progressive enrichment of MyoII specifically at the DV (vertical) junctions (Fig. 1h,i). The amplitude of MyoII polarity in the wild-type embryos tends to decrease over time (88,89). Interestingly, it significantly increased after 5HT2A overexpression compared to the wild-type embryos (Fig. 1j). In line with this, we observed more aligned DV-oriented junctions forming supracellular cables in 5HT2A overexpressing embryos (Fig. 1h and Extended Data Fig. 2h), indicating that the majority of DV-oriented junctions did not shrink; consistent with this hypothesis, there was a significant reduction in cumulative T1 events (Fig. 1l,m). However, local tissue extension was not significantly affected (Extended Data Fig. 2i) and cumulative rosettes were higher (Extended Data Fig. 2j,k). This suggests that the reduced T1 events in 5HT2A overexpression are compensated for by increased rosette formation, resulting in no significant effect on tissue extension.

Taken together, these results suggest a dose-dependent effect of 5HT2A on MyoII levels, polarity and spatial patterning. At zero levels of 5HT2A (in *5HT2A* mutants), junctional and medial MyoII levels were reduced and polarization was largely unaffected, whereas over-expression of 5HT2A led to enrichment of MyoII specifically at the DV oriented junctions, giving rise to hyper-polarization. Among the GPCRs known to activate MyoII in the ectoderm namely Smog (38) and Cirl (37), 5HT2A is the only GPCR that hyper-polarizes junctional MyoII when over-expressed. This raises the question of how the overexpression of 5HT2A hyper-polarizes the junctional MyoII. One possibility is that the 5HT2A localization is polarized and hence this imparts polarization to MyoII. To investigate the localization of 5HT2A, we generated a C-terminally tagged 5HT2A::mNeonGreen construct (Extended Data Fig. 3a) under the *sqh* promoter to have homogenous over-expression. MyoII was specifically recruited to the DV oriented junctions in 5HT2A::mNeonGreen overexpressing embryos, resulting in hyper-polarization similar to wild-type receptor over-expression (Extended Data Fig. 3b-d). 5HT2A::mNeonGreen was localized throughout the cell membrane as well as in the cytoplasmic organelle (Extended Data Fig. 3 e,f). These cytoplasmic organelles were endocytic vesicles, as they co-localized with dextran filled mobile endocytic vesicles (Extended Data Fig. 8a,a'). Significantly, the membrane localization of 5HT2A::mNeonGreen was not polarized (Extended Data Fig. 3e,f).

Serotonin signaling is permissive in the ectoderm

Since the localization of the receptor is not polarized, we next investigated the possibility that the receptor activation by the ligand is polarized. Tryptophan hydroxylase (hereafter Trh), is the rate-limiting enzyme involved in the biogenesis of serotonin (Fig. 2a), the bonafide ligand recognized by serotonin receptors and present at the beginning of germ band extension (28). We therefore investigated the null mutant Trh^{01} (44), in which the enzyme activity is impaired. Maternal and zygotic Trh^{01} mutant embryos develop normally, and this mutation has a mild effect on germ-band extension (data not shown). Maternal and zygotic knockout of Trh resulted in the specific reduction of the medial-apical MyoII levels (Fig. 2b,c and Video 4) with no significant changes in the junctional MyoII levels (Fig. 2b,d and Video 4). The reduction of medial MyoII was similar to that in 5HT2A mutant embryos (Fig. 1d,g). This suggests that serotonin is not required for junctional signalling under physiological conditions and that 5HT2A signaling at the junctions is serotonin independent, or that another ligand compensates for absence of serotonin. Medial apical MyoII levels are sensitive to the ligand dosage (overexpression of another ligand Fog which partially signals through Smog in the ectoderm, results in the hyperactivation of apical MyoII in the ectoderm; 52,38). To investigate the dose response of the serotonin, we studied the gain of Trh function by over-expressing wild-type Trh enzyme. We presume that this leads to elevated serotonin levels as reported elsewhere (53,54). Interestingly, MyoII levels in the DV oriented junctions were higher at all time points and the amplitude of polarity was significantly increased (Fig. 2e,f,g and Video 5), whereas medial MyoII levels did not increase at most time points (Fig. 2e,h). These results reveal the dose dependent effect of serotonin in the spatial control of MyoII recruitment.

Overexpression of both the ligand and the receptor is similar in hyper-polarizing junctional MyoII. Loss of both the ligand and the receptor is similar in reduction of medial MyoII levels. To further investigate whether serotonin functions via 5HT2A, we first asked if serotonin requires 5HT2A to hyper-activate junctional MyoII when Trh is overexpressed. To test this, we over-expressed Trh in 5HT2A mutant embryos and observed a reduction in both junctional and medial MyoII levels, similar to that observed in 5HT2A mutant embryos, and a loss of hyper-polarization (Fig. 2i-k and Video 7). We then asked whether 5HT2A mediated hyper-polarization requires serotonin. Following the over-expression of 5HT2A in Trh^{01} mutant embryos, junctional MyoII hyper-polarization was no longer observed (Fig. 2l,m,n and Video 6). Junctional MyoII levels were similar to WT embryos and medial MyoII levels were significantly reduced (Fig. 2l,m,o). These data are similar to the Trh^{01} mutant embryos (Fig. 2b-d). Taken together, these data argue that serotonin exerts its function through 5HT2A.

In conclusion, at physiological levels, serotonin and 5HT2A are essential for medial apical MyoII recruitment. At the junctions, serotonin is not essential at physiological levels to control MyoII (Fig. 2b,d), presumably due to redundancy with another ligand. However, serotonin functions via 5HT2A when either the ligand (serotonin) or the receptor is overexpressed (Fig. 2i-k and Fig. 2l-o) and such redundancy is no longer apparent. The fact that reduced serotonin synthesis does not perturb polarity at junctions also indicates that serotonin signaling is permissive in the ectoderm.

5HT2A sets the magnitude of Toll/Cirl polarity signaling

What could be the additional ligand recognized by 5HT2A at the junctions? Three Toll receptors, Toll 2, 6 and 8, impart the polarization of junctional MyoII (36,37). Toll receptor, for example Toll-8 and the adhesion GPCR Cirl/Latrophilin interact to form a complex, mutually attract each other and mediate MyoII polarization at the cell-cell interface (Fig. 3a and 37). We wanted to know whether Toll receptors instruct 5HT2A mediated hyper-

polarization. To this end, we knocked-down Toll 2,6,8 (by injecting *toll-2,6,8* RNAi) in 5HT2A over-expressing embryos and found a similar MyoII levels and polarity as in *toll-2,6,8* RNAi injected WT embryos (Fig. 3b-d and Video 8). We no longer observed hyper-polarization of MyoII (Fig. 3b,d and Video 8), suggesting that the Toll receptors are required for 5HT2A mediated amplification of MyoII polarity. Concomitantly, 5HT2A::mNeonGreen membrane localization was depleted following the knockdown of Toll-2,6,8 and accumulated in intracellular vesicles (Extended Data Fig. 4a,b), junctional MyoII levels and polarity were consistently reduced (Extended Data Fig. 4a,c). This suggests that, Toll receptors are required to recruit or stabilize 5HT2A to the membrane. Toll-8 interacts with Cirl and recruits MyoII at the cell-cell interface (37). We therefore investigated whether 5HT2A transduces Cirl polarized signalling. Both Cirl and 5HT2A null mutants were homozygous viable, however double-mutants were homozygous embryonic lethal. Interestingly, we observed that the heterozygous 5HT2A mutation enhanced the phenotype of the homozygous Cirl mutation with respect to the wild-type embryos (Fig. 3e-g). The levels of junctional MyoII (Fig. 3e,f) and the local tissue extension (Fig. 3g) were reduced compared to the wild-type embryos in both the homozygous Cirl mutant (*Cirl-/-*) and homozygous 5HT2A mutant (*5HT2A-/-*) embryos (Fig. 3e-f and tissue extension in 5HT2A mutant embryos in Extended Data Fig. 2a,b) alone; while in the homozygous Cirl mutant and heterozygous 5HT2A mutant embryos (*Cirl -/- 5HT2A-/+*), MyoII levels and local tissue extension were further reduced (Fig. 3e-g and Video 9). In contrast, heterozygous Cirl mutation (*Cirl -/+*) did not enhance homozygous 5HT2A mutation junctional MyoII phenotype (Fig. 3e,f). Taken together, these data suggest a synergistic or additive effect of Cirl and 5HT2A on junctional MyoII recruitment and tissue extension and that 5HT2A levels are critical. To investigate whether 5HT2A signals independently of Cirl, we over-expressed 5HT2A in Cirl mutant embryos (Fig. 3h-k). Strikingly, ectopic 5HT2A rescued the low levels of MyoII in Cirl mutant embryos, but not the planar polarity of MyoII (Fig. 3h-k and Video 10). In Cirl mutants, junctional MyoII levels were reduced at all time points (Fig. 3h,i), while polarity was significantly reduced only initially and remained low at later time points (Fig. 3j), and medial MyoII levels were significantly reduced at all time points (Fig. 3h,k). When 5HT2A was overexpressed in Cirl mutant embryos, junctional MyoII levels were similar to wild-type embryos (Fig. 3h,i) and medial MyoII levels were partially rescued (Figure 3h,k). Surprisingly, the amplitude of polarity remained low at most time points as in Cirl mutant embryos (Fig. 3j). This indicates that 5HT2A quantitatively controls the MyoII levels and extent of the Cirl-dependent planar polarity cue. While Cirl/Toll impart polarization per se, 5HT2A controls the magnitude of this effect but not polarity itself. Overall, we conclude that the 5HT2A forms a distinct signaling module that regulates the MyoII levels, while Toll/Cirl serves as polarizing signaling module.

5HT2A activates junctional Rho1/MyoII through Gβ13f/Gγ1 and Dp114RhoGEF

GPCR signaling activates MyoII through the Rho1 pathway (Fig. 4a and 38,39). We wanted to know whether 5HT2A signals through this pathway. We monitored the Rho1 activity over time using the Rho1 biosensor (64) in 5HT2A mutant embryos, and found the levels of Rho1-GTP were significantly reduced at both the junctions and medial-apically at all the time points (Fig. 4b-d and Video 11). The Rho1 amplitude of polarity was not significantly reduced (Fig. 4e). In 5HT2A gain-of-function embryos, junctional Rho1-GTP levels were initially not much different than in wild-type embryos, while at later time points, Rho1-GTP signals tended to decrease in the wild-type, whereas in 5HT2A overexpression, it remained significantly higher in all junctional orientations (Fig. 4f,g and Video 12), in contrast, MyoII was enriched specifically at DV-oriented junctions (Fig. 1h,i). We observed a slight but not significant increase in the Rho1-GTP polarity (Fig. 4h). To investigate this difference, we hypothesized that Rho1 signaling is further amplified downstream and studied the downstream effectors of

Rho1: Rho-associated kinase (Rok) and myosin phosphatase. We found that the overexpression of 5HT2A represses myosin phosphatase (Extended Data Fig. 5a,b and Video 13), which inhibits the de-phosphorylation of MyoII as revealed by monitoring the junctional recruitment of the myosin-binding subunit of myosin-phosphatase (MBS::GFP). This suggests that overexpression of 5HT2A enhances the stabilization of junctional MyoII, leading to hyper-polarization. To confirm that the emergence of hyper-polarization of junctional MyoII is dependent on Rok activity, we injected the Rok inhibitor H-1152 compound and we observed that upon this treatment the hyper-polarization of MyoII was lost (Extended Data Fig. 5c), confirming that the 5HT2A mediated hyper-activation of junctional MyoII requires Rok activity. Taken together, 5HT2A controls MyoII through the Rho1 signaling pathway.

Dp114RhoGEF compartmentalizes Rho1 activity at cell junctions (Fig.4a and 39,55). We asked whether the 5HT2A mediated activation of junctional Rho1/MyoII is dependent on Dp114RhoGEF. The endogenous levels of Dp114RhoGEF levels were significantly reduced in 5HT2A mutant embryos (Fig. 4i,j). Conversely, we observed elevated levels of Dp114RhoGEF at the junctions in 5HT2A over-expressing embryos (Fig. 4k,l). Furthermore, over-expression of the 5HT2A in Dp114RhoGEF knockdown embryos did not result in hyper-polarization of junctional MyoII (Fig. 4m-o). Junctional MyoII levels and the amplitude of polarity were reduced in a manner similar to Dp114RhoGEF knockdown embryos (Fig. 4m-o). These data confirm that the 5HT2A activates junctional MyoII through Dp114RhoGEF.

The heterotrimeric G-proteins $G\alpha_{12/13}$ Gβ13f/Gγ1 transduce GPCR signaling to modulate apical and junctional Rho1/MyoII activation (Fig.4a and 38,39). Gα-GTP activates apical Rho1/MyoII while Gβ13f/Gγ1 heterodimer activate junctional Rho1/MyoII. Gβ13f/Gγ1 over-expression hyper-activates junctional Rho1/MyoII (39) similar to 5HT2A over-expression. If 5HT2A signals through Gβ13f/Gγ1, removal of 5HT2A and over-expression of Gβ13f/Gγ1 should have no effect unless 5HT2A is required for the ectopic Gβ13f/Gγ1 activation. We therefore asked whether ectopic Gβ13f/Gγ1 mediated hyper-activation of MyoII requires 5HT2A. To examine this, we over-expressed Gβ13f/Gγ1 in the 5HT2A mutant embryos. Hyper-activation was lost and MyoII levels were reduced to intermediate levels between WT and 5HT2A mutant embryos (Fig. 4p,q). These data suggest that 5HT2A is required for Gβ13f/Gγ1 dependent activation of junctional MyoII. Given that Dp114RhoGEF mediates Gβ13f/Gγ1 signaling to activate junctional Rho1/MyoII (Fig. 4a and 39) and that 5HT2A requires Dp114RhoGEF (Fig. 4m-o), we conclude that 5HT2A signals through Gβ13f/Gγ1 and Dp114RhoGEF to activate junctional Rho1/MyoII. The mammalian ortholog of 5HT2A is known to activate PLC through the canonical GαQ signaling pathway that leads to accumulation of IP3, DAG and PKC (56,57). Here we find that 5HT2A activates Rho1/MyoII through a non-canonical Gβ13f/Gγ1 and Dp114RhoGEF signaling pathway.

5HT2B inhibits MyoII in the ectoderm and requires 5HT2A

All the experiments point to a key quantitative role of 5HT2A signaling in tuning the junctional activation of MyoII, whose polarization is imparted specifically by Toll/Cirl. This begs the question of how the level of signaling by 5HT2A is regulated. It has been reported that the mammalian 5HT2 class receptors (5HT2A, 5HT2B and 5HT2C) interact to form heterodimers (58), that bias the signaling of one protomer over the other. Since *Drosophila* lacks 5HT2C, we examined germ band extension in 5HT2B null mutant embryos (43, 44) and observed a delay of almost 15 minutes (Extended Data Fig. 1a,b and Video 1). Strikingly, MyoII levels were higher at the junctions as well as in the medial pool (Extended Data Fig. 6a,b,d and Video 14). Consistently, we observed a similar phenotype in embryos expressing short-hairpin RNA (shRNA) against 5HT2B (Extended Data Fig. 6e,f,h) and following injection of 5HT2B

double-stranded RNA (5HT2B dsRNA) (Fig. 5a,b,c and Video 15). These data suggest a repression of MyoII enrichment by this receptor. Amplitude of MyoII polarity was not affected (Fig. 5d and Extended Data Fig. 6c,g).

To investigate how 5HT2B inhibits MyoII accumulation, we considered the possibility that the inhibitory effect emerged from an interaction between 5HT2A and 5HT2B, consistent with reports in other systems (58). One could envision two possible interactions (Fig. 5e): 1) 5HT2A inhibits 5HT2B and 5HT2B inhibits MyoII per se. 2) 5HT2B inhibits 5HT2A and 5HT2A activates MyoII per se. Removal of the individual receptors does not distinguish between these two hypotheses, however, removal of both the receptors is predicted to have different outcomes. According to the first hypothesis, in the absence of 5HT2A, 5HT2B becomes constitutively active and represses MyoII. In double mutants, this will be similar to removing the repressor 5HT2B alone, with higher levels of MyoII. According to the second hypothesis, when 5HT2B is removed, 5HT2A becomes hyper-activated and activates more MyoII. But when both are removed, the situation will be similar to removing the activator 5HT2A with reduced levels of MyoII. To test these predictions, we injected 5HT2B dsRNA into the 5HT2A mutant embryos. MyoII levels were reduced as in the 5HT2A mutant embryos (Figure. 5f-h and Video 16), supporting the second hypothesis that 5HT2B inhibits 5HT2A and 5HT2A activates MyoII (Fig. 5i). This argues that 5HT2B requires 5HT2A to repress MyoII recruitment both at the junctions and medially.

5HT2A and 5HT2B interact to form heterocomplexes and undergo endocytosis

The above study demonstrated a genetic interaction between 5HT2A and 5HT2B. To further investigate whether 5HT2A and 5HT2B physically interact to form heterocomplexes, we used scanning Fluorescence Cross-Correlation Spectroscopy (sFCCS) (59,60) (Fig. 5 j-o) to access co-diffusion of 5HT2A and 5HT2B at the membrane *in vivo* (Fig. 5j). We developed a C-terminally tagged 5HT2B::mCherry construct (Extended Data Fig. 7a). The fluorescently labelled 5HT2B behaved like the wild-type receptor, as junctional MyoII remained unaffected and medial MyoII levels were reduced in both wild-type (Extended Data Fig. 7b-d) and fluorescently labelled (Extended Data Fig. 7e-g) receptors overexpression. 5HT2B::mCherry was localized to both the membrane and cytoplasmic organelles (Extended Data Fig. 7h,i). When co-expressed, 5HT2A::mNeonGreen and 5HT2B::mCherry co-localized both at the membrane and in cytoplasmic organelles (Extended Data Fig. 8c,c'). We performed sFCCS in embryos co-expressing 5HT2A::mNeonGreen and 5HT2B::mCherry and in negative control embryos co-expressing the Vesicular Stomatitis Virus G-protein tagged with mNeonGreen (VsVg::mNeonGreen) and 5HT2B::mCherry, two proteins that are not expected to interact (negative control). All the constructs were expressed under the *sqh* promoter to ensure homogenous and similar expression levels. FCCS analysis showed positive correlation for 5HT2A and 5HT2B (Fig. 5 l,m), whereas no evidence of correlation was detected in the negative control. This argues that the two proteins physically interact *in vivo* and form heterocomplexes. Notably, the detected cross-correlation (~0.3±0.1) is lower than the values (~0.4-0.8 depending on the choice of fluorophores) commonly detected on positive cross-correlation controls (61-63), i.e. for the case of 100% binding, indicating that the interaction of 5HT2A and 5HT2B is transient. By analyzing FCS amplitude in each channel (see materials and methods for details), a similar surface concentration of 5HT2A and 5HT2B was detected (Fig. 5n). Diffusion coefficients of ~0.5 $\mu m^2/s$ were estimated for individual receptors in both the negative controls and in the co-expression condition (Fig. 5o), arguing that heterodimers will have similar diffusion dynamics as free receptors. Taken together, the genetic interaction, co-localization and cross-correlation analyses confirm a functional and physical interaction between 5HT2A and 5HT2B *in vivo* (Fig. 5p).

Based on this, we then asked how 5HT2B inhibits 5HT2A. We found that most of the 5HT2A::mNeonGreen colocalized with the dextran filled endocytic vesicles while most of the 5HT2B::mCherry cytoplasmic organelle did not (Extended Data Fig. 8a,a',b,b'). Consistently, 5HT2A::mNeonGren cytoplasmic organelles were encapsulated in clathrin coated vesicles as accessed with the clathrin heavy chain (ChC)::RFPt (Extended Data Fig. 8d,d') and Rab5::GFP, which labels the early endosomes, did not colocalize with 5HT2B::mCherry cytoplasmic organelles (Extended Data Fig. 8e,e'). These observations suggest that 5HT2A undergoes endocytosis, while 5HT2B alone appears less likely to be internalized. Strikingly, when co-expressed, 5HT2A::mNeonGreen and 5HT2B::mCherry colocalize in the membrane and cytoplasmic organelles (Extended Data Fig. 8c,c'), consistent with the formation of heterocomplexes accessed by FCCS (Fig. 5l,m). Based on this observation, we hypothesized that 5HT2B promotes 5HT2A endocytosis and compared the surface levels and the number of endocytic vesicles of 5HT2A::mNeonGreen in varying dosage of 5HT2B: 5HT2B mutant and endogenous levels (Extended Data Fig. 8f,f',f''). In the absence of 5HT2B, the 5HT2A::mNeonGreen signal at the membrane was higher compared to when expressed in the context of endogenous 5HT2B levels (Extended Data Fig. 8f,f'), consistent with the increased MyoII levels in the absence of 5HT2B (Fig. 5a-c and Extended Data Fig. 6a,b,d,e,f,h). Conversely, the number of 5HT2A::mNeonGreen cytoplasmic vesicles per cell was lower (Extended Data Fig. 8f,f''). Most of the cytoplasmic vesicles in the endogenous levels of 5HT2B were endocytic vesicles as they colocalized with the dextran filled mobile endocytic vesicles (Extended Data Fig. 8a,a'). This argues that 5HT2B promotes 5HT2A internalization. Collectively, 5HT2B inhibits 5HT2A signaling through heterodimerization and subsequent endocytosis. 5HT2A::mNeonGreen is recruited to the membrane in the absence of 5HT2B, whereas membrane levels are depleted in the absence of Toll receptors and accumulated in cytoplasmic organelles (Extended Data Figure 4a,b), suggesting that Toll receptors are required to recruit or stabilize 5HT2A to the membrane and 5HT2B potentially regulates its membrane turnover/endocytosis.

Serotonin receptors are required for tissue flows and MyoII activation during chick gastrulation

To investigate whether the activation of MyoII by the 5HT-receptors signalling during development is evolutionarily conserved in vertebrates, we studied its function in the epiblast of gastrulating chick embryos (Fig. 6a). Serotonin has been detected in the chick embryo during the primitive streak formation (20). Pharmacological treatments targeting the serotonergic system have been shown to affect chick gastrulation (19,20,21). Contractile supracellular actomyosin cables are required to generate and integrate tissue scale deformations during chick gastrulation (33,34). We examined the distribution of phosphorylated MyoII during the primitive streak formation following the treatment with the 5HT2A/2B antagonist Ritanserin (Fig. 6b and Extended Data Fig. 12). Embryos were treated with different concentrations of the inhibitor (20μM, 100 μM, and 200μM). Phospho-MyoII levels were markedly reduced in the treated embryos both in the contractile region and in the extra-embryonic tissue (EE); area opaca (Fig. 6b and Extended Data Fig. 12). We observed a marked reduction in the phospho-MyoII signal at 20μM and an even greater reduction at 200μM (Fig. 6b). Tangential supracellular MyoII cables at the posterior margin drive oriented intercalation (33). Fewer cables were observed in treated embryos (Fig. 6b and Extended Data Fig 12). This suggests that 5HT2A/2B are required for the activation of MyoII during chick gastrulation. Consistent with this, we observed gastrulation defects such as: delayed primitive streak formation by 4-7 hours at lower concentrations (50μM Videos, data not shown), contraction of the extra-embryonic (EE) and embryo proper (EP) tissues, whereas in the untreated embryos the EE tissue expands steadily and the EP tissue maintains a constant area (34 and Video 18). Primitive

streak formation was absent in the embryos treated with 200 μM Ritanserin (Fig. 6c and Video 18). Large-scale vortex like tissue flows drive the primitive streak formation (33,34). In order to investigate whether these large-scale tissue flows were perturbed, we performed Particle Image Velocimetry (PIV) analysis (34) to follow the tissue motion in the brightfield movies. Consistently, no large-scale vortex like tissue flows were observed in the treated embryos (Fig. 6d and Video 19). Overall, we conclude that the role of serotonin receptors in activating actomyosin contractility and tissue flows during embryonic axis elongation is evolutionarily conserved in vertebrates.

Discussion

We have reported that serotonin signalling has an evolutionary conserved morphogenetic function during embryo gastrulation through the regulation of actomyosin contractility. We delineate two modes of regulation of MyoII activation by GPCRs in *Drosophila* (Extended Data Fig. 9): serotonin receptors control quantitatively Rho1, while planar polarization is controlled by Toll receptors together with Cirl/Latrophilin. Toll receptors encode polarity information and polarize Rho1/MyoII activity (Extended Data Fig. 10 and Video 17). Toll receptors such as Toll-8 interact with the adhesion GPCR Cirl/Latrophilin to form a self-organized polarizing module and recruit MyoII to the cell-cell interface (37). The GPCR Cirl signaling contributes to both MyoII levels by regulating F-actin (Extended Data Fig. 11 and Video 10) and to junctional MyoII polarization by interacting with Toll receptors. 5HT2A requires Toll receptors for surface recruitment and MyoII hyperpolarization when over-expressed, and shows redundancy with Cirl to regulate F-actin (Extended Data Fig. 11 and Video 10), however, signals independently of Cirl to form a distinct signaling module to regulate MyoII levels. 5HT2A/5HT2B physically interact to form heterocomplexes and regulate MyoII levels, forming a module that transduces quantitative information. Our data show that 5HT2B regulates the 5HT2A signaling and membrane levels through heterodimerization and endocytosis. Another GPCR, Smog, regulates the level of junctional Rho1/MyoII activation and signals independent of Fog at the junctions (38). Collectively, we conclude that multiple GPCRs are required to regulate MyoII levels. There is no single ligand that encodes quantitative information. Multiple GPCRs interpret specific ligand(s) and the ligand-receptor stoichiometry determined by homodimerization (65)/ heterodimerization and subsequent endocytosis, encode and integrate quantitative information.

We found that the serotonin/receptors signaling also activates MyoII contractility during chick gastrulation. How MyoII is activated during primitive streak formation in the chick is unknown. GPCR signaling instructs the activation of MyoII during axis extension in *Drosophila* (38,39). By studying two phylogenetically distant species (separated by ~250 million years), we uncovered the evolutionarily conserved morphogenetic function of serotonin and GPCR serotonin receptors in modulating cellular mechanics. Our finding opens a new door for the investigation of the serotonergic system in other organisms, such as sea urchin, zebrafish, *Xenopus* and mouse (2,17-26, 66, reviewed in 67), where the serotonergic system has been detected in early embryos and morphogenetic function has been documented in some organisms, but the mechanism remains elusive. Serotonin receptors and transporters have been detected in the human oocyte and in embryos four days after fertilization (68,69). These reports suggest a potential role for the serotonergic system in human development. Cellular mechanics plays a major role in maintaining tissue homeostasis and integrity during development and in the adult. Indeed, serotonin and serotonin receptors are expressed in a wide range of organs. Inhibition of serotonin receptors results in heart defects and incomplete neural tube closure in mouse (26) and chicken (19). Neural tube closure requires actomyosin contractility (70,71).

Our findings highlight the need to investigate the role of the serotonergic system beyond its classical physiological function in the nervous system.

GPCR signalling is involved in the regulation of actomyosin contractility during morphogenesis in several organisms. For example, Fog/Smog/Mist and Toll/Cirl in *Drosophila* (37,38,41,52), Wnt/Frzzled in C. elegans (72). Serotonin/5HT2A/5HT2B in *Drosophila* and chick, as we report in this study. All the metazoan G *alpha* family, including $G\alpha_{12/13,}$ which is known to regulate actomyosin contractility during gastrulation in *Drosophila* (38,73,74) and required for gastrulation in zebrafish (86), and GαQ (data on MyoII activation in *Drosophila* not shown), is conserved in the common metazoan ancestor (75). Our study highlights the evolutionarily conserved function of GPCR signalling in regulating actomyosin contractility and cellular mechanics during morphogenesis.

The presence of serotonin precedes the appearance of the nervous-system on both evolutionary and developmental time scales. Serotonin is present in unicellular eukaryotes that evolved more than 600 million years ago. For example, *Tetrahymena*, can produce and respond to serotonin and receptor inhibitor, that alters phagocytosis and ciliary motion, which requires actin-dependent contractility (76,77,78). Serotonin has been detected in primitive nerveless metazoans: sponges (79,80) that evolved nearly 500-600 million years ago (81); and has been shown to induce coordinated contractions (82) that require actomyosin (83). Insects evolved around ~440 million years ago, flying insects after 40 million years (84), birds evolved around 150 million years ago (85). By comparing the two species whose common ancestor lived 250 million years ago, we show the functional conservation of serotonin/receptors signaling in the regulation of actomyosin contractility during embryogenesis. Later, in the adult organisms, the serotonin signaling predominantly modulates organismal behavior. This provides strong evidence for a strategy implemented by evolution to repurpose a cellular mechanism contextually, without having to innovate a new mechanism completely from scratch. The serotonin signaling might have evolved primarily to regulate intracellular signaling, cellular contractility, and collective cell behavior and later evolved in the nervous system for inter-cellular communication.

Methods:

Detailed methods in supplementary.

Author contributions:

S.K. and T.L. conceived the project. S.K. performed all the experiments and quantifications except for sFCCS experiments presented in Fig. 5j-o performed by S.K. and V.D., and quantified by V.D., and chick experiments performed by S.K. and M.S., and quantified by M.S. (Fig. 6 and Extended Data Fig. 12). E.D.S. and J.-M.P. created all the fluorescent constructs and dsRNA. S.K., V.D., M.S. and T.L discussed the data. S.K. and T.L. wrote the manuscript and all authors made comments.

Acknowledgements:

This work benefited greatly from the stimulating discussions in the Lecuit team and thank all the lab members for their support during the course of the project. We are thankful to S. Kerridge for helpful discussions, inspiration for the project and performing initial screening of

the GPCRs. We are grateful to Leslie B. Vosshall (Rockefeller university, USA), David Krantz Lab (UCLA, USA), the Drosophila Genetic Resource Center and the Bloomington Stock Center for the gift of flies. We thank Cedric Maurange lab for providing lab space for chick experiments. We also thank Pierre-françois Lenne for access to infrastructure and lab space. The authors thank Salvatore Chiantia (University of Potsdam, Germany) for technical discussions about the sFCCS analysis. This work was supported by the ERC AdvGrant Biomecamorph (323027), the Ligue Nationale Contre le Cancer (Equipe labellisée 2018). S.K. was initially supported by a Ph.D. fellowship from the LabEx INFORM (ANR-11- LABX-0054) and of the A*MIDEX project (ANR-11-IDEX-0001-02), funded by the ''Investissements d'Avenir French Government program'' and from Ligue Nationale Contre le Cancer, *4ème année de thèse,* grant no. TDQD22642. We acknowledge the France-BioImaging infra-structure supported by the French National Research Agency (ANR–10–INBS- 04-01, Investments for the future.

Competing interests:

The authors declare no competing interests.

Data and materials availability:

The authors declare that the data supporting the findings of this study are available within the paper and its supplementary information files. Raw image data are available upon reasonable request.

Code availability:

The codes used for image analysis, sFCCS data analysis and PIV analysis are available upon request.

References:

1. Buznikov G. A. (1984). The action of neurotransmitters and related substances on early embryogenesis. *Pharmacology & therapeutics*, *25*(1), 23–59. https://doi.org/10.1016/0163-7258(84)90023-8
2. BUZNIKOV, G. A., CHUDAKOVA, I. V., & ZVEZDINA, N. D. (1964). THE R OLE OF NEUROHUMOURS IN EARLY EMBRYOGENESIS. I. SEROTONIN CONTENT OF DEVELOPING EMBRYOS OF SEA URCHIN AND LOACH. *Journal of embryology and experimental morphology*, *12*, 563–573.
3. Csaba G. (1993). Presence in and effects of pineal indoleamines at very low level of phylogeny. *Experientia*, *49*(8), 627–634. https://doi.org/10.1007/BF01923943
4. Essman E. J. (1987). The serotonergic system in Tetrahymena pyriformis. *La Ricerca in clinica e in laboratorio*, *17*(1), 77–82.
5. Csaba, G., Kovács, P., & Pállinger, E. (2007). How does the unicellular Tetrahymena utilise the hormones that it produces? Paying a visit to the realm of atto-and zeptomolar concentrations. *Cell and tissue research*, *327*(1), 199–203. https://doi.org/10.1007/s00441-005-0052-9
6. Turlejski K. (1996). Evolutionary ancient roles of serotonin: long-lasting regulation of activity and development. *Acta neurobiologiae experimentalis*, *56*(2), 619–636.

7. Buznikov, G. A., Lambert, H. W., & Lauder, J. M. (2001). Serotonin and serotonin-like substances as regulators of early embryogenesis and morphogenesis. *Cell and tissue research*, *305*(2), 177–186. https://doi.org/10.1007/s004410100408
8. Odjakova, M., & Hadjiivanova, C. (1997). ANIMAL NEUROTRANSMITTER SUBSTANCES IN PLANTS.
9. Pelagio-Flores, R., Ortíz-Castro, R., Méndez-Bravo, A., Macías-Rodríguez, L., & López-Bucio, J. (2011). Serotonin, a tryptophan-derived signal conserved in plants and animals, regulates root system architecture probably acting as a natural auxin inhibitor in Arabidopsis thaliana. *Plant & cell physiology*, *52*(3), 490–508. https://doi-org.insb.bib.cnrs.fr/10.1093/pcp/pcr006
10. Hannon, J., & Hoyer, D. (2008). Molecular biology of 5-HT receptors. *Behavioural brain research*, *195*(1), 198–213. https://doi.org/10.1016/j.bbr.2008.03.020
11. Barnes, N. M., & Sharp, T. (1999). A review of central 5-HT receptors and their function. *Neuropharmacology*, *38*(8), 1083–1152. https://doi.org/10.1016/s0028-3908(99)00010-6
12. Peroutka, S. J., & Howell, T. A. (1994). The molecular evolution of G protein-coupled receptors: focus on 5-hydroxytryptamine receptors. *Neuropharmacology*, *33*(3-4), 319–324. https://doi.org/10.1016/0028-3908(94)90060-4
13. Walker, R. J., Brooks, H. L., & Holden-Dye, L. (1996). Evolution and overview of classical transmitter molecules and their receptors. *Parasitology*, *113 Suppl*, S3–S33. https://doi.org/10.1017/s0031182000077878
14. Romero-Reyes, J., Molina-Hernández, A., Díaz, N. F., & Camacho-Arroyo, I. (2021). Role of serotonin in vertebrate embryo development. *Reproductive biology*, *21*(1), 100475. https://doi.org/10.1016/j.repbio.2020.100475
15. Hasan, A., Yeom, HS., Ryu, J. *et al.* Phenylethylamides derived from bacterial secondary metabolites specifically inhibit an insect serotonin receptor. *Sci Rep* **9**, 20358 (2019). https://doi.org/10.1038/s41598-019-56892-z
16. Berger, M., Gray, J. A., & Roth, B. L. (2009). The expanded biology of serotonin. *Annual review of medicine*, *60*, 355–366. https://doi.org/10.1146/annurev.med.60.042307.110802
17. Gustafson, T., & Toneby, M. (1970). On the role of serotonin and acetylcholine in sea urchin morphogenesis. *Experimental cell research*, *62*(1), 102–117. https://doi.org/10.1016/0014-4827(79)90512-3
18. Gutafson, T., & Toneby, M. I. (1971). How genes control morphogenesis. The role of serotonin and acetylcholine in morphogenesis. *American scientist*, *59*(4), 452–462.
19. Palén, K., Thörneby, L., & Emanuelsson, H. (1979). Effects of serotonin and serotonin antagonists on chick embryogenesis. *Wilhelm Roux's archives of developmental biology*, *187*(1), 89–103. https://doi.org/10.1007/BF00848170
20. Wallace J. A. (1982). Monoamines in the early chick embryo: demonstration of serotonin synthesis and the regional distribution of serotonin-concentrating cells during morphogenesis. *The American journal of anatomy*, *165*(3), 261–276. https://doi.org/10.1002/aja.1001650304
21. Fukumoto, T., Kema, I. P., & Levin, M. (2005). Serotonin signaling is a very early step in patterning of the left-right axis in chick and frog embryos. *Current biology : CB*, *15*(9), 794–803. https://doi.org/10.1016/j.cub.2005.03.044
22. Reisoli, E., De Lucchini, S., Nardi, I., & Ori, M. (2010). Serotonin 2B receptor signaling is required for craniofacial morphogenesis and jaw joint formation in

Xenopus. *Development (Cambridge, England)*, *137*(17), 2927–2937. https://doi.org/10.1242/dev.041079

23. Nikishin, D. A., Kremnyov, S. V., Konduktorova, V. V., & Shmukler, Y. B. (2012). Expression of serotonergic system components during early Xenopus embryogenesis. *The International journal of developmental biology*, *56*(5), 385–391. https://doi.org/10.1387/ijdb.113475dn
24. Beyer, T., Danilchik, M., Thumberger, T., Vick, P., Tisler, M., Schneider, I., Bogusch, S., Andre, P., Ulmer, B., Walentek, P., Niesler, B., Blum, M., & Schweickert, A. (2012). Serotonin signaling is required for Wnt-dependent GRP specification and leftward flow in Xenopus. *Current biology : CB*, *22*(1), 33–39. https://doi.org/10.1016/j.cub.2011.11.027
25. Sullivan, K. G., & Levin, M. (2016). Neurotransmitter signaling pathways required for normal development in Xenopus laevis embryos: a pharmacological survey screen. *Journal of anatomy*, *229*(4), 483–502. https://doi.org/10.1111/joa.12467
26. Choi, D. S., Ward, S. J., Messaddeq, N., Launay, J. M., & Maroteaux, L. (1997). 5-HT2B receptor-mediated serotonin morphogenetic functions in mouse cranial neural crest and myocardiac cells. *Development (Cambridge, England)*, *124*(9), 1745–1755. https://doi.org/10.1242/dev.124.9.1745
27. Colas, J. F., Launay, J. M., Kellermann, O., Rosay, P., & Maroteaux, L. (1995). Drosophila 5-HT2 serotonin receptor: coexpression with fushi-tarazu during segmentation. *Proceedings of the National Academy of Sciences of the United States of America*, *92*(12), 5441–5445. https://doi.org/10.1073/pnas.92.12.5441
28. Colas, J. F., Launay, J. M., & Maroteaux, L. (1999). Maternal and zygotic control of serotonin biosynthesis are both necessary for Drosophila germband extension. *Mechanisms of development*, *87*(1-2), 67–76. https://doi.org/10.1016/s0925-4773(99)00140-9
29. Colas, J. F., Launay, J. M., Vonesch, J. L., Hickel, P., & Maroteaux, L. (1999). Serotonin synchronises convergent extension of ectoderm with morphogenetic gastrulation movements in Drosophila. *Mechanisms of development*, *87*(1-2), 77–91. https://doi.org/10.1016/s0925-4773(99)00141-0
30. Irvine, K. D., & Wieschaus, E. (1994). Cell intercalation during Drosophila germband extension and its regulation by pair-rule segmentation genes. *Development (Cambridge, England)*, *120*(4), 827–841. https://doi.org/10.1242/dev.120.4.827
31. Bertet, C., Sulak, L., & Lecuit, T. (2004). Myosin-dependent junction remodelling controls planar cell intercalation and axis elongation. *Nature*, *429*(6992), 667–671. https://doi.org/10.1038/nature02590
32. Rauzi, M., Lenne, P. F., & Lecuit, T. (2010). Planar polarized actomyosin contractile flows control epithelial junction remodelling. *Nature*, *468*(7327), 1110–1114. https://doi.org/10.1038/nature09566
33. Rozbicki, E., Chuai, M., Karjalainen, A. I., Song, F., Sang, H. M., Martin, R., Knölker, H. J., MacDonald, M. P., & Weijer, C. J. (2015). Myosin-II-mediated cell shape changes and cell intercalation contribute to primitive streak formation. *Nature cell biology*, *17*(4), 397–408. https://doi.org/10.1038/ncb3138
34. Saadaoui, M., Rocancourt, D., Roussel, J., Corson, F., & Gros, J. (2020). A tensile ring drives tissue flows to shape the gastrulating amniote embryo. *Science (New York, N.Y.)*, *367*(6476), 453–458. https://doi.org/10.1126/science.aaw1965
35. Collinet, C., & Lecuit, T. (2021). Programmed and self-organized flow of information during morphogenesis. *Nature reviews. Molecular cell biology*, *22*(4), 245–265. https://doi.org/10.1038/s41580-020-00318-6

36. Paré, A. C., Vichas, A., Fincher, C. T., Mirman, Z., Farrell, D. L., Mainieri, A., & Zallen, J. A. (2014). A positional Toll receptor code directs convergent extension in Drosophila. *Nature*, *515*(7528), 523–527. https://doi.org/10.1038/nature13953
37. Lavalou, J., Mao, Q., Harmansa, S., Kerridge, S., Lellouch, A. C., Philippe, J. M., Audebert, S., Camoin, L., & Lecuit, T. (2021). Formation of polarized contractile interfaces by self-organized Toll-8/Cirl GPCR asymmetry. *Developmental cell*, *56*(11), 1574–1588.e7. https://doi.org/10.1016/j.devcel.2021.03.030
38. Kerridge, S., Munjal, A., Philippe, J. M., Jha, A., de las Bayonas, A. G., Saurin, A. J., & Lecuit, T. (2016). Modular activation of Rho1 by GPCR signalling imparts polarized myosin II activation during morphogenesis. *Nature cell biology*, *18*(3), 261–270. https://doi.org/10.1038/ncb3302
39. Garcia De Las Bayonas, A., Philippe, J. M., Lellouch, A. C., & Lecuit, T. (2019). Distinct RhoGEFs Activate Apical and Junctional Contractility under Control of G Proteins during Epithelial Morphogenesis. *Current biology : CB*, *29*(20), 3370–3385.e7. https://doi.org/10.1016/j.cub.2019.08.017
40. Vishwakarma, V., Le, T. P., & Chung, S. (2022). Multifunctional role of GPCR signaling in epithelial tube formation. *Development (Cambridge, England)*, *149*(15), dev200519. https://doi.org/10.1242/dev.200519
41. Manning, A. J., Peters, K. A., Peifer, M., & Rogers, S. L. (2013). Regulation of epithelial morphogenesis by the G protein-coupled receptor mist and its ligand fog. *Science signaling*, *6*(301), ra98. https://doi.org/10.1126/scisignal.2004427
42. Hanlon, C. D., & Andrew, D. J. (2015). Outside-in signaling--a brief review of GPCR signaling with a focus on the Drosophila GPCR family. *Journal of cell science*, *128*(19), 3533–3542. https://doi.org/10.1242/jcs.175158
43. Gasque, G., Conway, S., Huang, J., Rao, Y., & Vosshall, L. B. (2013). Small molecule drug screening in Drosophila identifies the 5HT2A receptor as a feeding modulation target. *Scientific reports*, *3*, srep02120. https://doi.org/10.1038/srep02120
44. Qian, Y., Cao, Y., Deng, B., Yang, G., Li, J., Xu, R., Zhang, D., Huang, J., & Rao, Y. (2017). Sleep homeostasis regulated by 5HT2b receptor in a small subset of neurons in the dorsal fan-shaped body of drosophila. *eLife*, *6*, e26519. https://doi.org/10.7554/eLife.26519
45. Colas, J. F., Launay, J. M., & Maroteaux, L. (1999). Maternal and zygotic control of serotonin biosynthesis are both necessary for Drosophila germband extension. *Mechanisms of development*, *87*(1-2), 67–76. https://doi.org/10.1016/s0925-4773(99)00140-9
46. Collinet, C., Rauzi, M., Lenne, P. F., & Lecuit, T. (2015). Local and tissue-scale forces drive oriented junction growth during tissue extension. *Nature cell biology*, *17*(10), 1247–1258. https://doi.org/10.1038/ncb3226
47. Lye, C. M., Blanchard, G. B., Naylor, H. W., Muresan, L., Huisken, J., Adams, R. J., & Sanson, B. (2015). Mechanical Coupling between Endoderm Invagination and Axis Extension in Drosophila. *PLoS biology*, *13*(11), e1002292. https://doi.org/10.1371/journal.pbio.1002292
48. Blankenship, J. T., Backovic, S. T., Sanny, J. S., Weitz, O., & Zallen, J. A. (2006). Multicellular rosette formation links planar cell polarity to tissue morphogenesis. *Developmental cell*, *11*(4), 459–470. https://doi.org/10.1016/j.devcel.2006.09.007
49. Kasza, K. E., Farrell, D. L., & Zallen, J. A. (2014). Spatiotemporal control of epithelial remodeling by regulated myosin phosphorylation. *Proceedings of the National Academy of Sciences of the United States of America*, *111*(32), 11732–11737. https://doi.org/10.1073/pnas.1400520111

50. Tetley, R. J., Blanchard, G. B., Fletcher, A. G., Adams, R. J., & Sanson, B. (2016). Unipolar distributions of junctional Myosin II identify cell stripe boundaries that drive cell intercalation throughout Drosophila axis extension. *eLife*, *5*, e12094. https://doi.org/10.7554/eLife.12094
51. Kale, G. R., Yang, X., Philippe, J. M., Mani, M., Lenne, P. F., & Lecuit, T. (2018). Distinct contributions of tensile and shear stress on E-cadherin levels during morphogenesis. *Nature communications*, *9*(1), 5021. https://doi.org/10.1038/s41467-018-07448-8
52. Dawes-Hoang, R. E., Parmar, K. M., Christiansen, A. E., Phelps, C. B., Brand, A. H., & Wieschaus, E. F. (2005). folded gastrulation, cell shape change and the control of myosin localization. *Development (Cambridge, England)*, *132*(18), 4165–4178. https://doi.org/10.1242/dev.01938
53. Yuan, Q., Joiner, W. J., & Sehgal, A. (2006). A sleep-promoting role for the Drosophila serotonin receptor 1A. *Current biology : CB*, *16*(11), 1051–1062. https://doi.org/10.1016/j.cub.2006.04.032
54. Dierick, H. A., & Greenspan, R. J. (2007). Serotonin and neuropeptide F have opposite modulatory effects on fly aggression. *Nature genetics*, *39*(5), 678–682. https://doi.org/10.1038/ng2029
55. Silver, J. T., Wirtz-Peitz, F., Simões, S., Pellikka, M., Yan, D., Binari, R., Nishimura, T., Li, Y., Harris, T. J. C., Perrimon, N., & Tepass, U. (2019). Apical polarity proteins recruit the RhoGEF Cysts to promote junctional myosin assembly. *The Journal of cell biology*, *218*(10), 3397–3414. https://doi.org/10.1083/jcb.201807106
56. Roth, B. L., Nakaki, T., Chuang, D. M., & Costa, E. (1984). Aortic recognition sites for serotonin (5HT) are coupled to phospholipase C and modulate phosphatidylinositol turnover. *Neuropharmacology*, *23*(10), 1223–1225. https://doi.org/10.1016/0028-3908(84)90244-2
57. Roth, B. L., Willins, D. L., Kristiansen, K., & Kroeze, W. K. (1998). 5-Hydroxytryptamine2-family receptors (5-hydroxytryptamine2A, 5-hydroxytryptamine2B, 5-hydroxytryptamine2C): where structure meets function. *Pharmacology & therapeutics*, *79*(3), 231–257. https://doi.org/10.1016/s0163-7258(98)00019-9
58. Moutkine, I., Quentin, E., Guiard, B. P., Maroteaux, L., & Doly, S. (2017). Heterodimers of serotonin receptor subtypes 2 are driven by 5-HT_{2C} protomers. *The Journal of biological chemistry*, *292*(15), 6352–6368. https://doi.org/10.1074/jbc.M117.779041
59. Ries, J., Yu, S. R., Burkhardt, M., Brand, M., & Schwille, P. (2009). Modular scanning FCS quantifies receptor-ligand interactions in living multicellular organisms. *Nature methods*, *6*(9), 643–645. https://doi.org/10.1038/nmeth.1355
60. Dunsing, V., & Chiantia, S. (2018). A Fluorescence Fluctuation Spectroscopy Assay of Protein-Protein Interactions at Cell-Cell Contacts. *Journal of visualized experiments : JoVE*, (142), 10.3791/58582. https://doi.org/10.3791/58582
61. Foo, Y. H., Naredi-Rainer, N., Lamb, D. C., Ahmed, S., & Wohland, T. (2012). Factors affecting the quantification of biomolecular interactions by fluorescence cross-correlation spectroscopy. *Biophysical journal*, *102*(5), 1174–1183. https://doi.org/10.1016/j.bpj.2012.01.040
62. Dunsing, V., Mayer, M., Liebsch, F., Multhaup, G., & Chiantia, S. (2017). Direct evidence of amyloid precursor-like protein 1 *trans* interactions in cell-cell adhesion platforms investigated via fluorescence fluctuation spectroscopy. *Molecular biology of the cell*, *28*(25), 3609–3620. https://doi.org/10.1091/mbc.E17-07-0459

63. Dunsing, V., Petrich, A., & Chiantia, S. (2021). Multicolor fluorescence fluctuation spectroscopy in living cells via spectral detection. *eLife*, *10*, e69687. https://doi.org/10.7554/eLife.69687
64. Munjal, A., Philippe, J. M., Munro, E., & Lecuit, T. (2015). A self-organized biomechanical network drives shape changes during tissue morphogenesis. *Nature*, *524*(7565), 351–355. https://doi.org/10.1038/nature14603
65. Jha, A., van Zanten, T. S., Philippe, J. M., Mayor, S., & Lecuit, T. (2018). Quantitative Control of GPCR Organization and Signaling by Endocytosis in Epithelial Morphogenesis. *Current biology : CB*, *28*(10), 1570–1584.e6. https://doi.org/10.1016/j.cub.2018.03.068
66. Côté, F., Fligny, C., Bayard, E., Launay, J. M., Gershon, M. D., Mallet, J., & Vodjdani, G. (2007). Maternal serotonin is crucial for murine embryonic development. *Proceedings of the National Academy of Sciences of the United States of America*, *104*(1), 329–334. https://doi.org/10.1073/pnas.0606722104
67. Romero-Reyes, J., Molina-Hernández, A., Díaz, N. F., & Camacho-Arroyo, I. (2021). Role of serotonin in vertebrate embryo development. *Reproductive biology*, *21*(1), 100475. https://doi.org/10.1016/j.repbio.2020.100475
68. Neilson, L., Andalibi, A., Kang, D., Coutifaris, C., Strauss, J. F., 3rd, Stanton, J. A., & Green, D. P. (2000). Molecular phenotype of the human oocyte by PCR-SAGE. *Genomics*, *63*(1), 13–24. https://doi.org/10.1006/geno.1999.6059
69. Kaihola, H., Yaldir, F. G., Hreinsson, J., Hörnaeus, K., Bergquist, J., Olivier, J. D., Åkerud, H., & Sundström-Poromaa, I. (2016). Effects of Fluoxetine on Human Embryo Development. *Frontiers in cellular neuroscience*, *10*, 160. https://doi.org/10.3389/fncel.2016.00160
70. Galea, G. L., Cho, Y. J., Galea, G., Molè, M. A., Rolo, A., Savery, D., Moulding, D., Culshaw, L. H., Nikolopoulou, E., Greene, N. D. E., & Copp, A. J. (2017). Biomechanical coupling facilitates spinal neural tube closure in mouse embryos. *Proceedings of the National Academy of Sciences of the United States of America*, *114*(26), E5177–E5186. https://doi.org/10.1073/pnas.1700934114
71. Escuin, S., Vernay, B., Savery, D., Gurniak, C. B., Witke, W., Greene, N. D., & Copp, A. J. (2015). Rho-kinase-dependent actin turnover and actomyosin disassembly are necessary for mouse spinal neural tube closure. *Journal of cell science*, *128*(14), 2468–2481. https://doi.org/10.1242/jcs.164574
72. Lee, J. Y., Marston, D. J., Walston, T., Hardin, J., Halberstadt, A., & Goldstein, B. (2006). Wnt/Frizzled signaling controls C. elegans gastrulation by activating actomyosin contractility. *Current biology : CB*, *16*(20), 1986–1997. https://doi.org/10.1016/j.cub.2006.08.090
73. Parks, S., & Wieschaus, E. (1991). The Drosophila gastrulation gene concertina encodes a G alpha-like protein. *Cell*, *64*(2), 447–458. https://doi.org/10.1016/0092-8674(91)90652-f
74. Nikolaidou, K. K., & Barrett, K. (2004). A Rho GTPase signaling pathway is used reiteratively in epithelial folding and potentially selects the outcome of Rho activation. *Current biology : CB*, *14*(20), 1822–1826. https://doi.org/10.1016/j.cub.2004.09.080
75. de Mendoza, A., Sebé-Pedrós, A., & Ruiz-Trillo, I. (2014). The evolution of the GPCR signaling system in eukaryotes: modularity, conservation, and the transition to metazoan multicellularity. *Genome biology and evolution*, *6*(3), 606–619. https://doi.org/10.1093/gbe/evu038

76. Csaba, G., Kovács, P., & Pállinger, E. (2007). How does the unicellular Tetrahymena utilise the hormones that it produces? Paying a visit to the realm of atto-and zeptomolar concentrations. *Cell and tissue research*, *327*(1), 199–203. https://doi.org/10.1007/s00441-005-0052-9
77. Quiñones-Maldonado, V., & Renaud, F. L. (1987). Effect of biogenic amines on phagocytosis in Tetrahymena thermophila. *The Journal of protozoology*, *34*(4), 435–438. https://doi.org/10.1111/j.1550-7408.1987.tb03208.x
78. Williams, N. E., Tsao, C. C., Bowen, J., Hehman, G. L., Williams, R. J., & Frankel, J. (2006). The actin gene ACT1 is required for phagocytosis, motility, and cell separation of Tetrahymena thermophila. *Eukaryotic cell*, *5*(3), 555–567. https://doi.org/10.1128/EC.5.3.555-567.2006
79. Lentz TL: Histochemical Localization of Neurohumors in a Sponge. Journal of Experimental Biology. 1966, 162: 171-180.
80. Weyrer, S., Rutzler, K., & Rieger, R. (1999). Serotonin in Porifera? Evidence from developing Tedania ignis, the Caribbean fire sponge (Demospongiae). *MEMOIRS-QUEENSLAND MUSEUM*, *44*, 659-666.
81. Yin, Z., Zhu, M., Davidson, E. H., Bottjer, D. J., Zhao, F., & Tafforeau, P. (2015). Sponge grade body fossil with cellular resolution dating 60 Myr before the Cambrian. *Proceedings of the National Academy of Sciences of the United States of America*, *112*(12), E1453–E1460. https://doi.org/10.1073/pnas.1414577112
82. Ellwanger, K., Nickel, M. Neuroactive substances specifically modulate rhythmic body contractions in the nerveless metazoon *Tethya wilhelma* (Demospongiae, Porifera). *Front Zool* **3**, 7 (2006). https://doi.org/10.1186/1742-9994-3-7
83. Colgren, J., & Nichols, S. A. (2022). MRTF specifies a muscle-like contractile module in Porifera. *Nature communications*, *13*(1), 4134. https://doi.org/10.1038/s41467-022-31756-9
84. Misof, B., Liu, S., Meusemann, K., Peters, R. S., Donath, A., Mayer, C., Frandsen, P. B., Ware, J., Flouri, T., Beutel, R. G., Niehuis, O., Petersen, M., Izquierdo-Carrasco, F., Wappler, T., Rust, J., Aberer, A. J., Aspöck, U., Aspöck, H., Bartel, D., Blanke, A., … Zhou, X. (2014). Phylogenomics resolves the timing and pattern of insect evolution. *Science (New York, N.Y.)*, *346*(6210), 763–767. https://doi.org/10.1126/science.1257570
85. Brusatte, S. L., O'Connor, J. K., & Jarvis, E. D. (2015). The Origin and Diversification of Birds. *Current biology : CB*, *25*(19), R888–R898. https://doi.org/10.1016/j.cub.2015.08.003
86. Lin, F., Sepich, D. S., Chen, S., Topczewski, J., Yin, C., Solnica-Krezel, L., & Hamm, H. (2005). Essential roles of G{alpha}12/13 signaling in distinct cell behaviors driving zebrafish convergence and extension gastrulation movements. *The Journal of cell biology*, *169*(5), 777–787. https://doi.org/10.1083/jcb.200501104
87. Pilot, F., Philippe, J. M., Lemmers, C., Chauvin, J. P., & Lecuit, T. (2006). Developmental control of nuclear morphogenesis and anchoring by charleston, identified in a functional genomic screen of Drosophila cellularisation. *Development (Cambridge, England)*, *133*(4), 711–723. https://doi-org.insb.bib.cnrs.fr/10.1242/dev.02251

Fig.1 | 5HT2A is required for cell intercalation and MyoII accumulation in the *Drosophila* ectoderm.

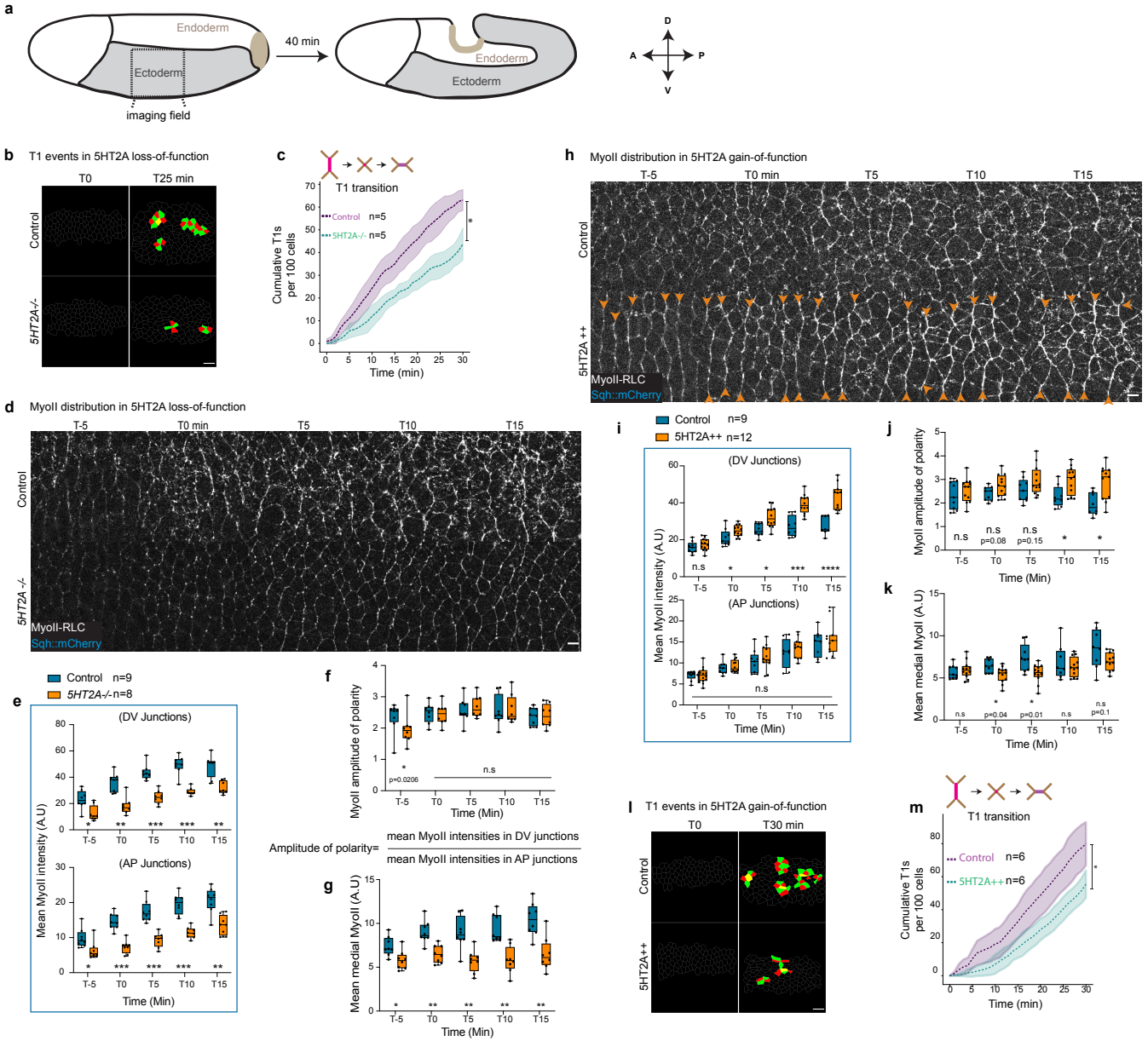

Fig. 1 | 5HT2A is required for cell intercalation and MyoII accumulation in the *Drosophila* ectoderm.

a) Ectoderm morphogenesis during *Drosophila* axis extension. (**b-c**) T1 events in 5HT2A loss-of-function. Representative images of T1s in control (top panels) and 5HT2A mutant (*5HT2A-/-*) (bottom panels) taken at T0 (left) and T25 min (right) (**b**) and quantification of cumulative T1s in the respective conditions (**c**). (**d-g**) MyoII distribution in 5HT2A loss-of-function in the region outlined in **a**. Live images of MyoII every 5 minutes interval, upper panels: control, lower panels: *5HT2A-/-* (**d**). Quantification of mean MyoII intensities in DV oriented and AP oriented junctions (**e**), amplitude of polarity (**f**) and mean medial-apical MyoII intensity (**g**) over time. **(h-k)** MyoII distribution in 5HT2A overexpression (5HT2A++). Live images of MyoII over-time, upper panels: control, lower panels: 5HT2A++, orange arrowheads showing the hyper-polarization of junctional MyoII (**h**). Quantification of MyoII intensities in DV oriented and AP oriented junctions (**i**), amplitude of polarity (**j**) and mean medial MyoII intensities (**k**). (**l-m**) T1 events in 5HT2A gain-of-function. Representative images of the T1 events taken at T0 (left) and T30 min (right) for control (upper panels) and 5HT2A++ (lower panels) (**l**) and quantification of cumulative T1 events in the respective conditions (**m**). ns: $p>0.05$, * $p< 0.05$, ** $p<0.005$, *** $p<0.0005$, **** $p<0.00005$ from Mann-Whitney test. n=number of embryos. Scale bars in **b** and **l** 10 μm, in **d** and **h** 5 μm.

Fig. 2 | Serotonin signaling is permissive in the ectoderm.

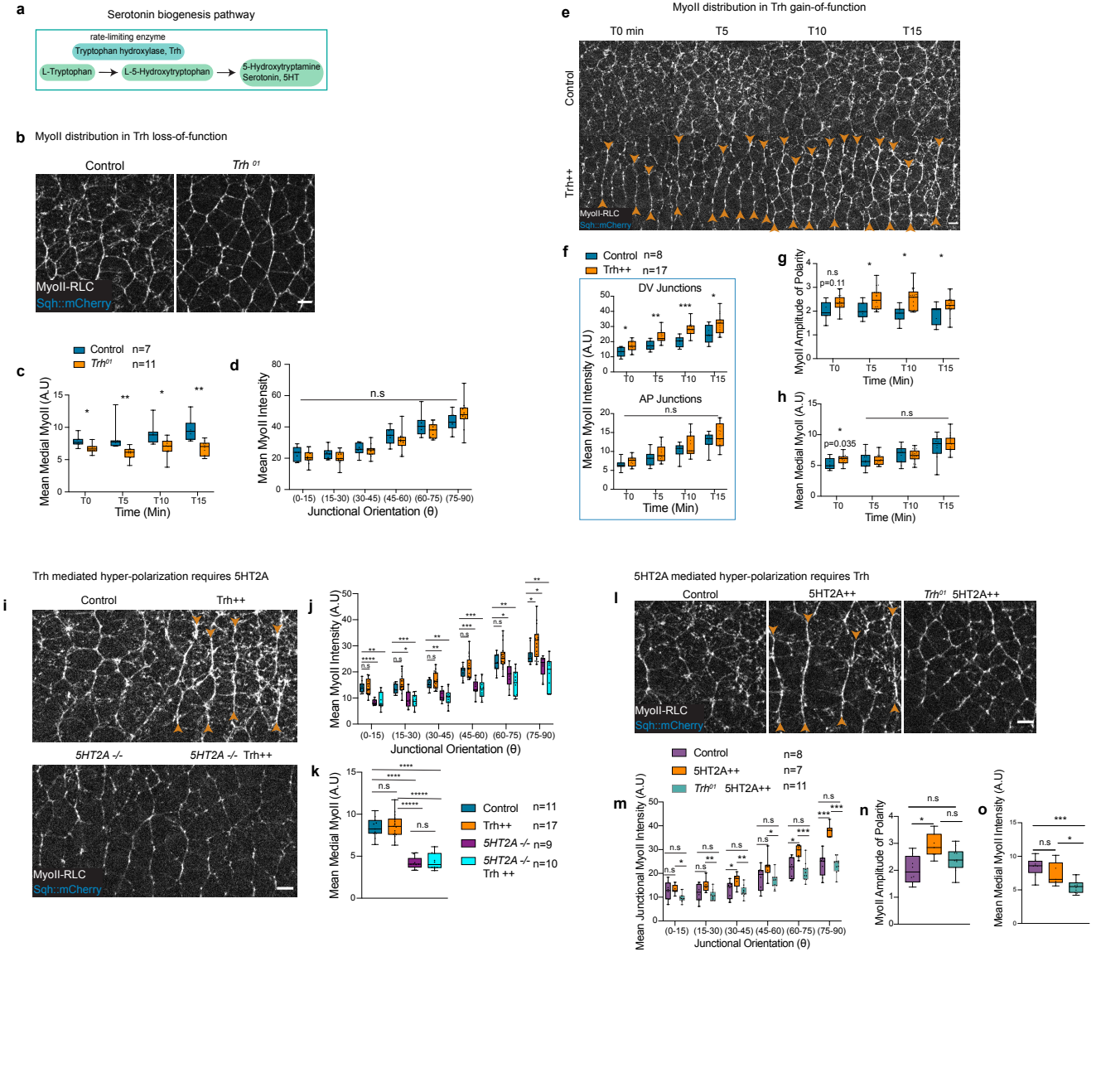

Fig. 2 | Serotonin signaling is permissive in the ectoderm.
a) Schematic of serotonin biogenesis, tryptophan hydroxylase (Trh) is the rate limiting enzyme. (**b-d**); **b**) Snapshot of MyII in Trh loss-of-function (*Trh*^{01} mutant); control (left panel) and *Trh*^{01} (right panel). Quantification of mean medial-apical MyoII levels over-time (**c**) and an example of the distribution of junctional MyoII intensities in different junctional orientations for different conditions (**d**). (**e-h**) Time-lapse of MyoII in Trh gain-of-function (Trh++), top panels: control, lower panels: Trh++, orange arrowheads indicate hyper-polarization of junctional MyoII (**e**). Quantification of MyoII intensities over-time in DV and AP oriented junctions (**f**), amplitude of polarity (**g**), and medial MyoII intensities (**h**). (**i-k**) Trh++ and *5HT2A-/-*. MyoII in control (top left), Trh++ (top right, orange arrowheads indicate hyper-polarization), *5HT2A-/-* (bottom left) and *5HT2A-/-* Trh++ (bottom right) (**i**). Quantification of junctional (**j**), and medial MyoII (**k**) intensities in different conditions. (**l-o**) *Trh*^{01} and 5HT2A++, MyoII in control (left panel), 5HT2A++ (middle panel, orange arrowheads indicate hyper-polarization) and *Trh*^{01} 5HT2A++ (right panel) (**l**), quantification of junctional MyoII intensities (**m**), amplitude of polarity (**n**), and medial MyoII (**o**) in different genotypes. ns: $p>0.05$, * $p< 0.05$, ** $p<0.005$, *** $p<0.0005$, **** $p<0.00005$, ***** $p<0.000005$ from Mann-Whitney test. n=number of embryos. Scale bars 5 μm.

Fig. 3 | 5HT2A amplifies Toll/Cirl polarity cue.

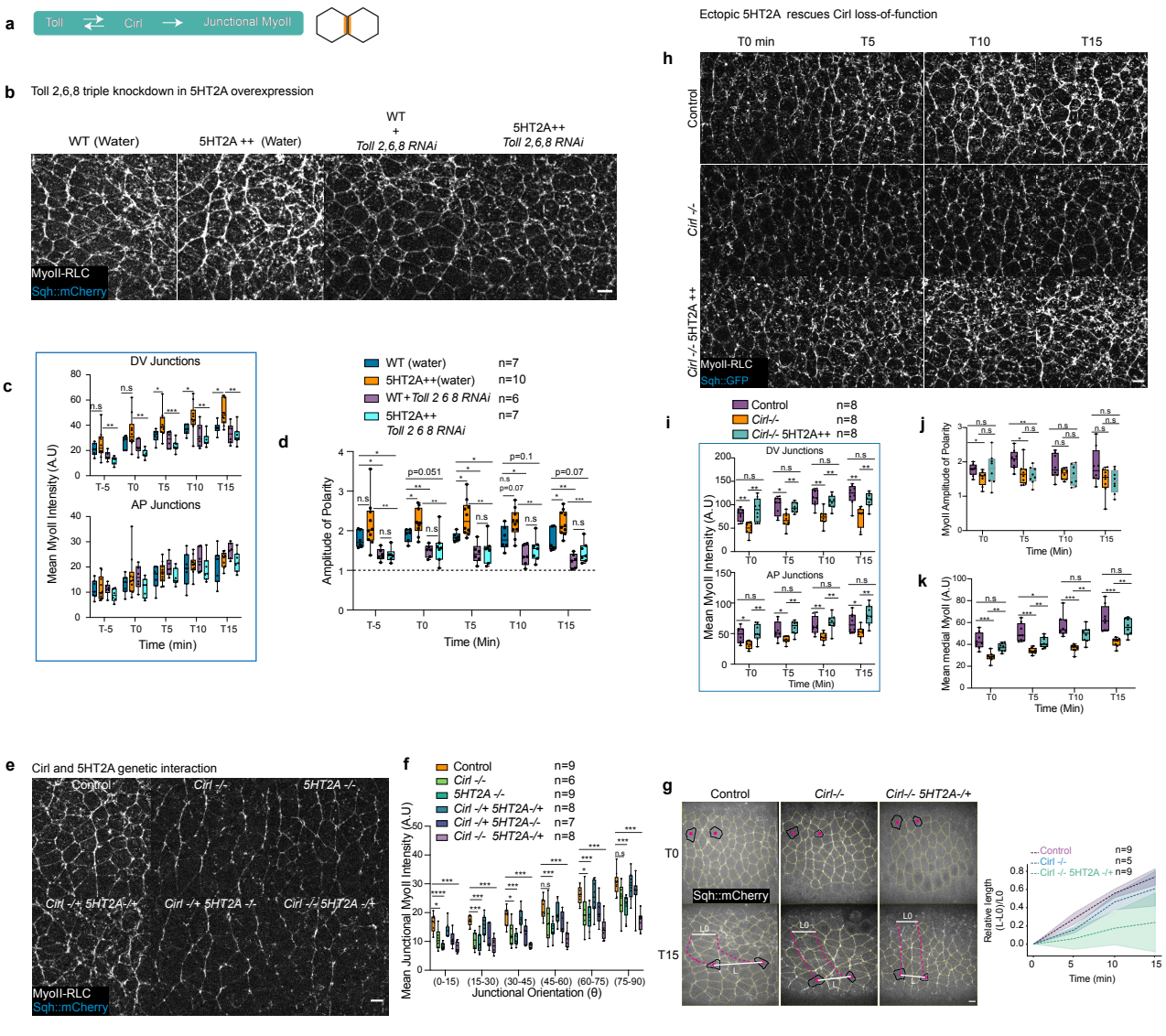

Fig. 3 | 5HT2A amplifies Toll/Cirl polarity cue.
a) Schematic showing Toll/Cirl mutual attraction activating MyoII at the cell-cell interface. (**b-d**) 5HT2A over-expression and Toll-2,6,8 knock-down. (**b**) MyoII images in different conditions (from left to right respectively): water injected WT, water injected 5HT2A++, Toll 2,6,8 triple RNAi injected WT, and Toll 2,6,8 triple RNAi injected 5HT2A++ embryos. Quantification of MyoII intensities in DV and AP oriented junctions over-time (**c**), amplitude of polarity (**d**) in different conditions. (**e-f**) Genetic interaction between Cirl and 5HT2A. **e**) MyoII snapshots in control (top-left), *Cirl-/-* (top-middle), *5HT2A-/-* (top-right), *Cirl-/+ 5HT2A-/+* (bottom-left), *Cirl-/+ 5HT2A-/-* (bottom-middle) and *Cirl-/- 5HT2A-/+* (bottom-right). **f**) Quantification of junctional MyoII intensities in different genotypes. **g**) Quantification of local tissue extension. Centroid of the cells outlined in dark tacked for 15 min starting 30 minutes after cellularization front passes the nucleus, pink dotted line is the track of the centroids. The relative length (L-L0)/L0 is plotted on the right. (**h-k**) 5HT2A overexpression in *Cirl-/-* showing 5HT2A rescuing MyoII levels in *Cirl-/-*. **h**) MyoII images at different time points (left to right), in different genotypes (top to bottom): control (top panel), Cirl-/- (middle panel) and Cirl-/- 5HT2A++ (bottom panel). Quantification of time traces of MyoII intensities in DV and AP oriented junctions (**i**), amplitude of polarity (**j**), and medial MyoII intensities (**k**) in different genotypes. ns: $p>0.05$, * $p< 0.05$, ** $p<0.005$, *** $p<0.0005$ from Mann-Whitney test. n=number of embryos. Scale bars 5 μm.

Fig. 4 | 5HT2A activates Rho1/MyoII through Gβ13f/Gγ1 and Dp114RhoGEF at the junctions.

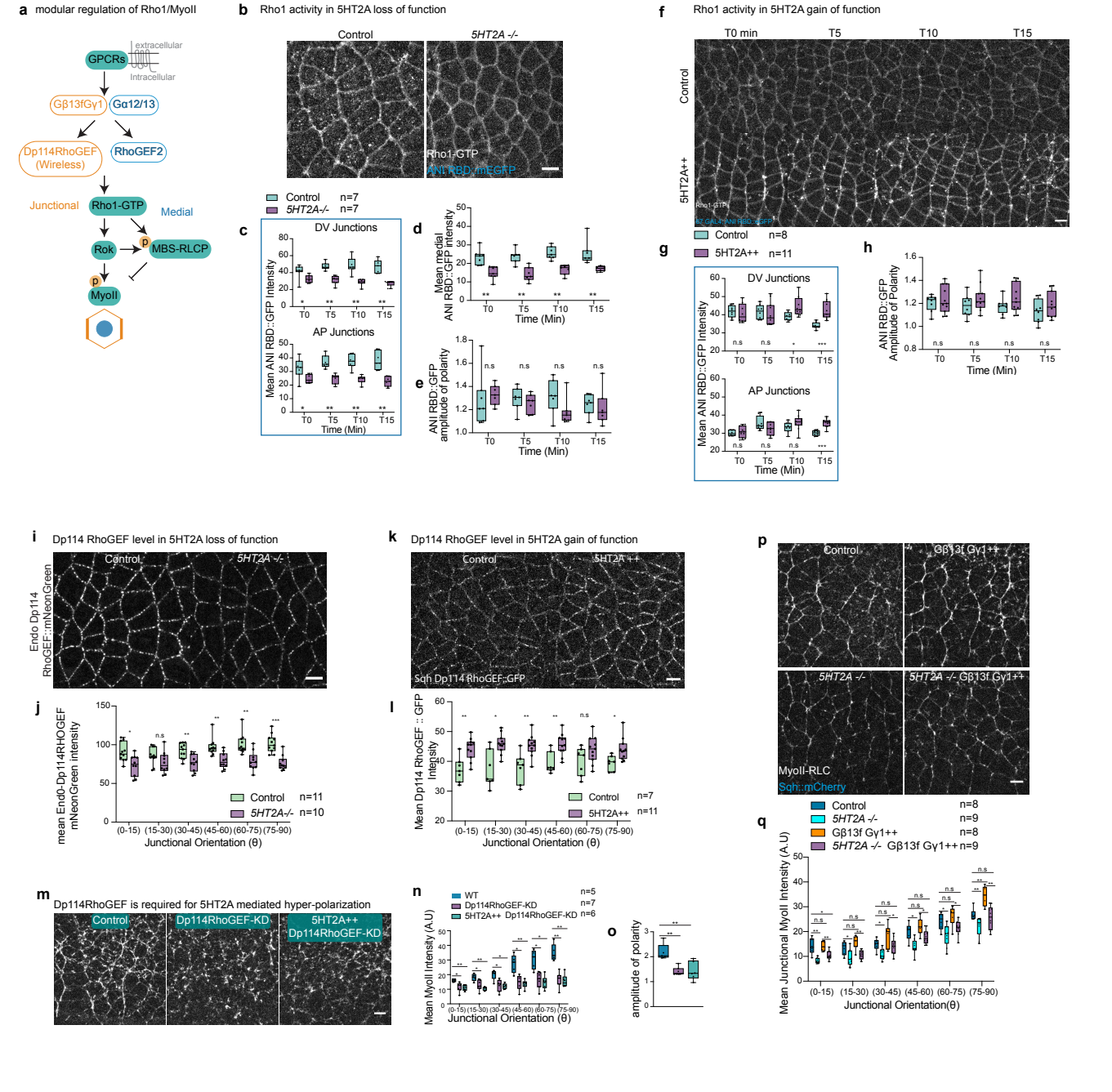

Fig. 4 | 5HT2A activates junctional MyoII through Gβ13f/Gγ1, Dp114RhoGEF and Rho1. **a**) Schematic showing GPCR signalling modules that activate junctional and medial Rho1/MyoII. (**b-e**) Rho1 activity in 5HT2A loss-of-function. Rho1-GTP snapshots in control (left panel) and *5HT2A-/-* (right panel) (**b**). Quantification of Rho-GTP sensor signal over time in DV and AP oriented junctions (**c**), medial-apically (**d**), and amplitude of polarity (**e**) in different conditions. (**f-h**) Rho1 activity in 5HT2A over-expression. Images of Rho1-GTP at different time points (left to right) and different genotypes (top to bottom): control (top panel), 5HT2A++ (bottom panel) (**f**). Quantification of Rho1-GTP sensor signal in DV and AP oriented junctions (**g**), and amplitude of polarity (**h**) over-time. (**i-l**) Dp114RhoGEF levels in *5HT2A-/-* and 5HT2A++. Snapshot of endogenous distribution of Dp114RhoGEF::mNeonGreen in control (left panel) and *5HT2A-/-* (right panel) (**i**); and quantification of signal in the respective genotypes (**j**). Snapshots of *sqh*-Dp114RhoGEF::GFP in control (left panel), and 5HT2A++(right panel) (**k**); and quantification of the junctional signals (**l**) in the respective genotypes. (**m-o**) MyoII distribution in 5HT2A over-expression and Dp114RhoGEF knock-down. Still images of MyoII in control (left), Dp114RhoGEF knock-down (middle), and Dp114RhoGEF knock-down 5HT2A over-expression (right) (**m**). Quantification of junctional MyoII intensities (**n**), and amplitude of polarity (**o**) for the above genotypes. (**p-q**) Gβ13f/Gγ1 over-expression in 5HT2A-/-. MyoII images in control (top-left), Gβ13f/Gγ1 ++ (top-right), *5HT2A-/-* (bottom-left) and *5HT2A-/-* Gβ13f/Gγ1++ (bottom-right) (**p**). Quantification of junctional MyoII in different genotypes (**q**). ns: $p>0.05$, * $p< 0.05$, ** $p<0.005$, *** $p<0.0005$, **** $p<0.00005$ from Mann-Whitney test. n=number of embryos. Scale bars 5 μm.

Fig. 5 | 5HT2B represses MyoII accumulation in the ectoderm and requires 5HT2A

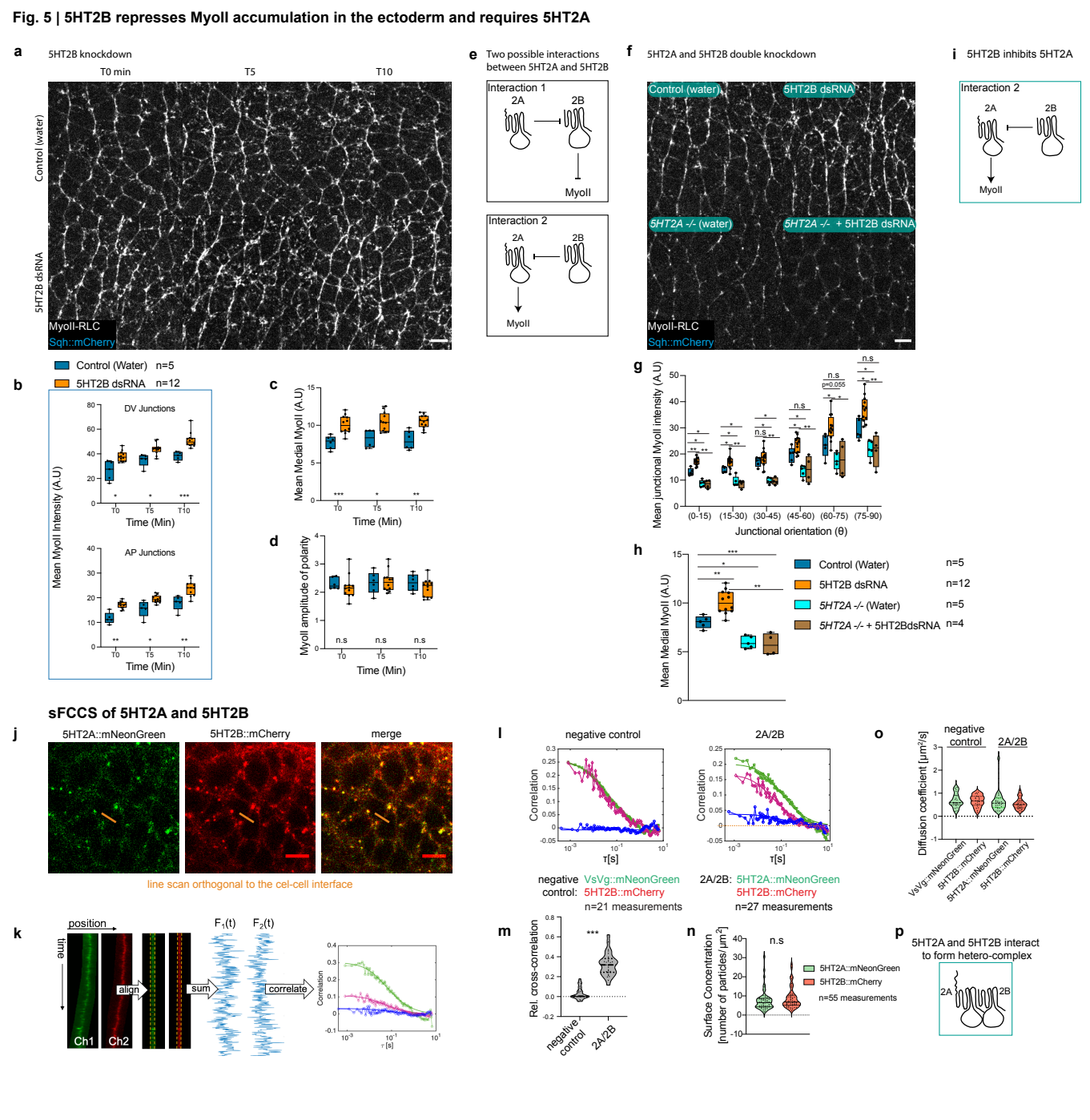

Fig. 5 | 5HT2B represses MyoII accumulation in the ectoderm and requires 5HT2A. (**a-d**) MyoII distribution in 5HT2B knock-down by RNAi (5HT2B dsRNA) injection. Images of MyoII for different time points (left to right); in water injected control (top panels) and 5HT2B dsRNA injection (bottom panels) (**a**). Quantification of time-traces of MyoII in DV and AP oriented junctions (**b**), medial MyoII (**c**), and amplitude of polarity (**d**). **e**) Schematic depicting two possible interactions between 5HT2A and 5HT2B. (**f-h**) Genetic interaction between 5HT2A and 5HT2B by knocking down 5HT2B in *5HT2A-/-*. MyoII images for water injected control (top-left), 5HT2B dsRNA (top-right), water injected *5HT2A-/-* (bottom-left) and *5HT2A-/-* injected with 5HT2B dsRNA (bottom-right) (**f**). Quantification of junctional (**g**), and medial (**h**) MyoII intensities for different conditions. (**i**) Schematic showing the 5HT2B inhibition of 5HT2A as supported by the genetic interaction above. (**j-p**) sFCCS of 5HT2A and 5HT2B. **j**) Confocal microscopy images of cells co-expressing 5HT2A::mNeonGreen and 5HT2B::mCherry. Scanning FCCS (sFCCS) measurements were performed perpendicular to the plasma membrane, as shown (orange line). **k**) Schematic of sFCCS. Line scans acquired sequentially in line interleaved mode were aligned computationally to correct for lateral cell or tissue movement. Membrane pixels were identified and integrated to provide membrane fluorescence time series in each channel. Autocorrelation functions (ACFs, green/red) in each channel and the cross-correlation function (CCF, blue) between two channels were calculated. **l**) Representative correlation functions obtained in a negative control sample consisting of a line co-expressing VsVg::mNeonGreen and 5HT2B::mCherry (left) and in cells co-expressing the two receptors 5HT2A::mNeonGreen and 5HT2B::mCherry (2A/2B) (right). In the negative control, the CCF fluctuates around zero, indicating absence of co-diffusion and thus hetero-interactions. In the 2A/2B sample, a positive CCF is obtained, indicating a co-diffusing species, i.e. the presence of hetero-complexes. **m**) Quantification of the relative cross-correlation in negative control and 5HT2A::mNeonGreen and 5HT2B::mCherry (2A/2B) co-expressing embryos. **n**) Quantification of surface concentration of 5HT2A::mNeonGreen and 5HT2B::mCherry. **o**) Quantification of diffusion coefficient in different conditions. **p**) Schematic showing the interaction between 5HT2A and 5HT2B. ns: $p>0.05$, * $p< 0.05$, ** $p<0.005$, *** $p<0.0005$ from Mann-Whitney test. n=number of embryos. For sFCCS n= number of independent measurements. Scale bars 5 μm.

Fig. 6 | Effect of serotonin receptor inhibition on tissue flows and myosin activity during chick gastrulation

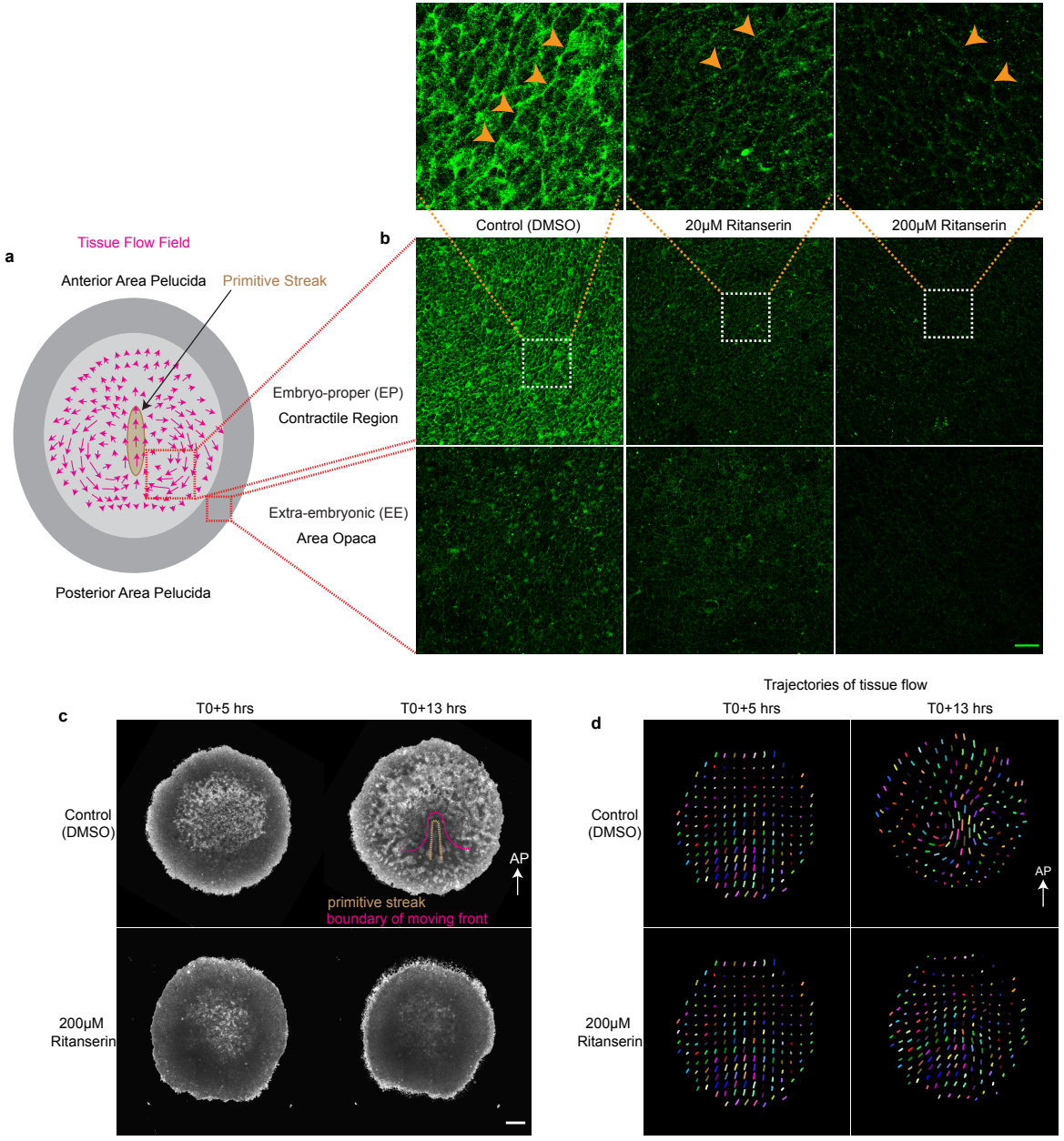

Fig. 6 | Effect of serotonin receptor inhibition on tissue flows and myosin activity during chick gastrulation.

a) Schematic of the gastrulating chick embryo**. b)** Images of phospho-MyoII in the embryo-proper (EP), contractile region (top panels) and extra embryonic tissue (EE), area opaca (bottom panels) in the control (left), 20 µM (middle) and 200 µM (right) Retanserin treated embryos. The white box in the images is magnified in the panels above each condition. The orange arrowheads indicate supracellular MyoII cables along the aligned cell junctions. The green scale bar is 50 µm. **c**) Snapshot of the brightfield images taken from the Video 18 at T0+5 hrs (left) and T0+13 hrs (right). Control treated with DMSO (top panels) and Ritanserin 200 µM (bottom panels). The white scale bar is 500 µm. **d**) Particle Image Velocimetry (PIV) images of the embryos in Video 18 at T0+5 hrs (left) and T0+13 hrs (right). PS: Primitive streak. The AP arrow in **c** and **d** indicates the direction of anterior posterior axis. The pink dotted line in **c** is the boundary of the tissue flow traced from the PIV image of the corresponding time in **d**.

Materials and Methods

Fly strains and genetics:

MyoII dynamics were visualized with *sqh-sqh::mCherry* except for Fig. 3h-k and Extended Data Fig. 7e-g, *sqh-sqh::GFP* lines were used. *5HT2A-GAL4, 5HT2B-GAL4* (ref. 43,44) (were gift from Leslie B. Vosshall, Rockefeller university, USA). *UAS-5HT2A* (BDSC#24504), *UAS-Trh* (BDSC#27638 and BDSC#27639), Trh^{01}(BDSC#86147; ref. 44), *sqh-5HT2A::mNeonGreen* and *sqh-5HT2B::mCherry* (generated in the laboratory). *Endo-Dp114RhoGEF::mNeonGreen* (generated in the lab), *67GAL4,sqh-Dp114RhoGEF::GFP* (ref. 39), *ANI-RBD::mEGFP, ANI-RBD::eGFP*(ref. 64), *ANI-RBD::mNeonGreen,sqhCherry* line (generated in the lab), *UAS-Gβ13f* and *UAS-Gγ1* (ref. 39), *UAS-5HT2B* (gift from David Krantz Lab UCLA, USA; ref. 44). Homozygous *Ecad::GFP,sqh-sqh::mCherry* line was used to visualize MyoII in *5HT2A-/-* (Fig.1a), Trh^{01} (Fig. 2b), *5HT2B-/-* (Extended Data Fig. 6a-d) and for 5HT2B dsRNA injection (Fig. 5a-d and f-h). All the over-expression experiments to visualize MyoII except for Fig. 3h-k, were done with *67GAL4,Ecad::GFP; sqh-sqh::mCherry* line (ref. 39). All the genetic crosses are detailed below.

Fly genetics by figures:

Fig. 1:
(b-g)
Control: ;*Ecad::GFP,sqh-sqh::mCherry;/;Ecad::GFP,sqh-sqh::mCherry;* (males and females);
5HT2A-/-: *5HT2A-GAL4* null mutant on third chromosome combined with *Ecad::GFP,sqh-sqh::mCherry* on the second chromosome. Embryos obtained from the homozygous (;*Ecad::GFP,sqh-sqh::mCherry/Ecad::GFP,sqh-sqh::mCherry;5HT2A-GAL4/5HT2A-GAL4*) males and females were imaged.

(h-m)
Control: *;67GAL4,Ecad::GFP,sqh-sqh::mCherry/+* (females) crossed with *yw* (males);
5HT2A++: *;67GAL4,Ecad::GFP,sqh-sqh::mCherry/UAS-5HT2A;* (females) crossed with homozygous *;UAS-5HT2A/UAS-5HT2A;* (males)

Fig. 2:
(b-d)
Control: *;Ecad::GFP,sqh-sqh::mCherry/Ecad::GFP,sqh-sqh::mCherry*; (males and females);
Trh^{01}: Trh^{01} null mutant on the third chromosome combined with *;Ecad::GFP,sqh-sqh::mCherry;* on the second chromosome. Embryos obtained from the homozygous (*;Ecad::GFP,sqh-sqh::mCherry/Ecad::GFP,sqh-sqh::mCherry;* Trh^{01}/Trh^{01}) males and females were imaged.

(e-h)
Control: *;67GAL4,Ecad::GFP,sqh-sqh::mCherry/+* (females) crossed with *yw* (males);
Trh++: *;67GAL4,Ecad::GFP,sqh-sqh::mCherry/UAS-Trh;* (females) crossed with homozygous *;UAS-Trh/UAS-Trh;* (males)

(i-k)
Control: *;67GAL4,Ecad::GFP,sqh-sqh::mCherry/+* (females) crossed with *yw* (males);

Trh++: *;67GAL4,Ecad::GFP,sqh-sqh::mCherry/UAS-Trh;* (females) crossed with homozygous *;UAS-Trh/UAS-Trh;* (males)
5HT2A-/-: *;67GAL4,Ecad::GFP,sqh-sqh::Cherry/+;5HT2A-GAL4/5HT2A-GAL4* (females) crossed with *;;5HT2A-GAL4/5HT2A-GAL4* (males)
5HT2A-/- Trh++: *;67GAL4,Ecad::GFP,sqh-sqh::mCherry/UAS-Trh;5HT2A-GAL4/5HT2A-GAL4* (females) crossed with homozygous *;UAS-Trh/UAS-Trh; 5HT2A-GAL4/5HT2A-GAL4* (males)

(l-o)
Control: *;67GAL4,Ecad::GFP,sqh-sqh::mCherry/+* (females) crossed with *yw* (males);
5HT2A++: *;67GAL4,Ecad::GFP,sqh-sqh::mCherry/UAS-5HT2A;* (females) crossed with ;UAS-5HT2A; (males)
Trh^{01} 5HT2A++: *;67GAL4,Ecad::GFP,sqh-sqh::mCherry/UAS-5HT2A;* Trh^{01}/Trh^{01} (females) crossed with *;UAS-5HT2A/UAS-5HT2A;* Trh^{01}/Trh^{01} (males)

Fig. 3:
(b-d)
WT (water): *;67GAL4,Ecad::GFP,sqh-sqh::mCherry/+* (females) crossed with *yw* (males);
5HT2A++ (water): *;67GAL4,Ecad::GFP,sqh-sqh::mCherry/UAS-5HT2A;* (females) crossed with *;UAS-5HT2A;* (males)
WT + Toll2,6,8 RNAi: *;67GAL4,Ecad::GFP,sqh-sqh::mCherry/+* (females) crossed with *yw* (males);
5HT2A++ + Toll2,6,8 RNAi: *;67GAL4,Ecad::GFP,sqh-sqh::mCherry/+* (females) crossed with *yw* (males);

(e-g)
Control: *;sqh-sqh::mCherry/sqh-sqh::mCherry;* (females) crossed with *yw* (males)
Cirl-/-: *;sqh-sqh::mCherry,* $Cirl^{KO}$*/sqh-sqh::mCherry,* $Cirl^{KO}$*;* (females) crossed with *;*$Cirl^{KO}/Cirl^{KO}$*;* (males)
5HT2A-/-: *;sqh-sqh::mCherry/+; 5HT2A-GAL4/5HT2A-GAL4* (females) crossed with *; 5HT2A-GAL4/5HT2A-GAL4;* (males)
Cirl-/+ 5HT2A-/+: *;sqh-sqh::mCherry,* $Cirl^{KO}$*/+; 5HT2A-GAL4/+* (females) crossed with *yw* (males)
Cirl-/+ 5HT2A-/-: *;sqh-sqh::mCherry,* $Cirl^{KO}$*/+; 5HT2A-GAL4/5HT2A-GAL4* (females) crossed with *;;5HT2A-GAL4/5HT2A-GAL4* (males)
Cirl-/- 5HT2A-/+: *;sqh-sqh::mCherry,* $Cirl^{KO}$*/* $Cirl^{KO}$*; 5HT2A-GAL4/+* (females) crossed with *;*$Cirl^{KO}/Cirl^{KO}$*;* (males)

(h-k)
Control: *;67GAL4/+;sqh-sqh::GFP,Lifeact::mCherry/+* (females) crossed with *;67GAL4/67GAL4;* (males)
Cirl -/-: *;*$Cirl^{KO}$*/67GAL4,*$Cirl^{KO}$*; sqh-sqh::GFP,Lifeact::mCherry/+* (females) crossed with *;67GAL4,*$Cirl^{KO}$*/67GAL4,*$Cirl^{KO}$*;* (males)
Cirl-/- 5HT2A++: *;67GAL4,*$Cirl^{KO}$*/67GAL4,*$Cirl^{KO}$*; sqh-sqh::GFP,Lifeact::mCherry/UAS-5HT2A* (females) crossed with *; 67GAL4,*$Cirl^{KO}$*/67GAL4,*$Cirl^{KO}$*; UAS-5HT2A/UAS-5HT2A* (males)

Fig. 4:
(b-e)
Control: *;UBI-ANI-RBD::mEGFP/ UBI-ANI-RBD::mEGFP;* females and males
5HT2A-/-: *;UBI-ANI-RBD::mEGFP/ UBI-ANI-RBD::mEGFP; 5HT2A-GAL4/5HT2A-GAL4* females and males

(f-h)
Control: *;67GAL4/+; UBI-ANI-RBD::eGFP/+* (females) crossed with *yw* (males)
5HT2A++: *;67GAL4/UAS-5HT2A; UBI-ANI-RBD::eGFP/+* (females) crossed with *;UAS-5HT2A/UAS-5HT2A;* (males)

(i-j)
Control: *;EndoDp114RhoGEF::mNeonGreen/ EndoDp114RhoGEF::mNeonGreen;* (males crossed with females)
5HT2A-/-: *;EndoDp114RhoGEF::mNeonGreen;/EndoDp114RhoGEF::mNeonGreen;5HT2A-GAL4/5HT2A-GAL4* (males crossed with females)

(k-l)
Control: *;67GAL4/+; sqh-eGFP::Dp114RhoGEF/+* (females) crossed with *yw* (males)
5HT2A++: *;67GAL4/UAS-5HT2A; sqh-eGFP::Dp114RhoGEF/+* (females) crossed with *;UAS-5HT2A/UAS-5HT2A;* (males)

(m-o)
Control: *;67GAL4,EcadGFP,sqh-sqh::mCherry/+* (females) crossed with *yw* (males);
Dp114RhoGEF-KD: *;67GAL4,Ecad::GFP,sqh-sqh::mCherry/UAS-Dp114RhoGEF-shRNA* (females) crossed with *;UAS-Dp114RhoGEF-shRNA/ UAS-Dp114RhoGEF-shRNA;* (males);
Dp114RhoGEF-KD 5HT2A++: *;67GAL4,Ecad::GFP,sqh-sqh::mCherry/UAS-Dp114RhoGEF-shRNA;UAS-5HT2A/+* (females) crossed with *;UAS-Dp114RhoGEF-shRNA/ UAS-Dp114RhoGEF-shRNA; UAS-5HT2A/UAS-5HT2A* (males);

(p-q)
Control: *;67GAL4,Ecad::GFP,sqh-sqh::mCherry/+* (females) crossed with *yw* (males);
5HT2A-/-: *;67GAL4,Ecad::GFP,sqh-sqh::mCherry/+;5HT2A-GAL4/5HT2A-GAL4* (females) crossed with *;;5HT2A-GAL4/5HT2A-GAL4* (males)
Gβ13f Gγ1++: *;67GAL4,Ecad::GFP,sqh-sqh::mCherry/UAS- Gβ13f;UAS- Gγ1/+* (females) crossed with *;UAS- Gβ13f/ UAS- Gβ13f;UAS- Gγ1/ UAS- Gγ1* (males)
5HT2A-/- Gβ13f Gγ1++: *;67GAL4,Ecad::GFP,sqh-sqh::mCherry/UAS- Gβ13f;5HT2A-GAL4,UAS- Gγ1/ 5HT2A-GAL4,UAS- Gγ1* (females) crossed with *;UAS- Gβ13f/ UAS- Gβ13f;5HT2A-GAL4,UAS- Gγ1/ 5HT2A-GAL4,UAS- Gγ1* (males)

Fig.5:
(a-d)
Control: *;Ecad::GFP,sqh-sqh::mCherry/Ecad::GFP,sqh-sqh::mCherry;* males and females
5HT2B dsRNA: *;Ecad::GFP,sqh-sqh::mCherry/Ecad::GFP,sqh-sqh::mCherry;* males and females

(f-h)
Control: *;Ecad::GFP,sqh-sqh::mCherry/Ecad::GFP,sqh-sqh::mCherry;* males and females
5HT2B dsRNA: *;Ecad::GFP,sqh-sqh::mCherry/Ecad::GFP,sqh-sqh::mCherry;* males and females

5HT2A-/-: *;Ecad::GFP,sqh-sqh::mCherry/Ecad::GFP,sqh-sqh::mCherry; 5HT2A-GAL4/5HT2A-GAL4* males and females
5HT2A-/- 5HT2BdsRNA: *;Ecad::GFP,sqh-sqh::mCherry/Ecad::GFP,sqh-sqh::mCherry; 5HT2A-GAL4/5HT2A-GAL4* males and females

(**l-o**)
negative control: *sqh-VsVg::mNeonGreen/sqh-5HT2B::mCherry* (males and females)
2A/2B: *;sqh-5HT2A::mNeonGreen/ sqh-5HT2A::mNeonGreen; sqh-5HT2B::mCherry/ sqh-5HT2B::mCherry* (males and females)

Extended Data Fig. 1:
(a-b)
WT: *yw* males and females
5HT2A-/-: *;;5HT2A-GAL4/5HT2A-GAL4* males and females
5HT2B-/-: *;;5HT2B-GAL4/5HT2B-GAL4* males and females

Extended Data Fig. 2:
(a-c, e-g)
Control: ;*Ecad::GFP,sqh-sqh::mCherry;/;Ecad::GFP,sqh-sqh::mCherry;* (males and females)

5HT2A-/-: (;*Ecad::GFP,sqh::mCherry/Ecad::GFP,sqh-sqh::mCherry;5HT2A-GAL4/5HT2A-GAL4*

(**d, h-k**)
Control: *;67GAL4/+; sqh-eGFP::Dp114RhoGEF/+* (females) crossed with *yw* (males)
5HT2A++: *;67GAL4/UAS-5HT2A; sqh-eGFP::Dp114RhoGEF/+* (females) crossed with *;UAS-5HT2A/UAS-5HT2A;* (males)

Extended Data Fig. 3:
(b-d)
Control: *;;sqh-sqh::mCherry/ sqh-sqh::mCherry* males and females
sqh-5HT2A::neonGreen: *; sqh-5HT2A::mNeonGreen/ sqh-5HT2A::mNeonGreen;sqh-sqh::mCherry/ sqh-sqh::mCherry* males and females

(e-f)
;*sqh*-5HT2A::mNeonGreen/ *sqh*-5HT2A::mNeonGreen; *sqh*-GAP43::mCherry/*sqh*-GAP43::mCherry (males and females)

Extended Data Fig. 4:
;*sqh*-5HT2A::mNeonGreen/ *sqh*-5HT2A::mNeonGreen; *sqh-sqh*::mCherry/ *sqh-sqh*::mCherry

Extended Data Fig. 5:
(a-b)
Control: *;UAS-MBS::GFP/67GAL4;* (females) crossed with *;67GAL4/67GAL4;* (males)
5HT2A++: *;UAS-MBS::GFP/67GAL4;UAS-5HT2A/* + (females) crossed with *;67GAL4/67GAL4;* (males)
(**c**)

;*sqh*-5HT2A::mNeonGreen/ *sqh*-5HT2A::mNeonGreen; *sqh-sqh*::mCherry/ *sqh-sqh*::mCherry

Extended Data Fig. 6:
(a-d)
Control: ;*Ecad::GFP,sqh-sqh::mCherry;/;Ecad::GFP,sqh-sqh::mCherry;* (males and females);
5HT2B-/-: *5HT2B-GAL4* null mutant on third chromosome combined with *Ecad::GFP,sqh-sqh::mCherry* on the second chromosome. Embryos obtained from the (;*Ecad::GFP,sqh::mCherry/Ecad::GFP,sqh-sqh::mCherry;5HT2B-GAL4/TM6B,hum*) males and females were imaged. We did not observe homozygous adults when combined with ;*Ecad::GFP,sqh::mCherry/Ecad::GFP,sqh-sqh::mCherry;* line.
(e-h)
Control: *;67GAL4,Ecad::GFP,sqh-sqh::mCherry/+* (females) crossed with *yw* (males);
5HT2BshRNA: *;67GAL4,Ecad::GFP,sqh-sqh::mCherry/UAS-5HT2B shRNA;* (females) crossed with homozygous *;UAS-5HT2B-shRNA/UAS-5HT2B-shRNA;* (males)

Extended Data Fig. 7:
(b-d)
Control: *;67GAL4,Ecad::GFP,sqh-sqh::mCherry/+* (females) crossed with *yw* (males);
5HT2B-WT++: *;67GAL4,Ecad::GFP,sqh-sqh::mCherry/UAS-5HT2B-WT;* (females) crossed with homozygous *;UAS-5HT2B-WT/UAS-5HT2B-WT;* (males)

(e-g)
Control: *;sqh-sqh::GFP/ sqh-sqh::GFP;* (males and females)
5HT2B::mCherry++: *;sqh-sqh::GFP/ sqh-sqh::GFP; sqh-5HT2B::mCherry/ sqh-5HT2B::mCherry* (males and females)

(h-i)
;sqh-5HT2B::mCherry/ sqh-5HT2B::mCherry;

Extended Data Fig. 8:
(a,a')
;*sqh-5HT2A::mNeonGreen/ sqh-5HT2A::mNeonGreen*; (males and females)

(b,b')
;;sqh-5HT2B::mCherry/sqh-5HT2B::mCherry (males and females)

(c,c') ;*sqh-5HT2A::mNeonGreen/ sqh-5HT2A::mNeonGreen; sqh-5HT2B::mCherry/ sqh-5HT2B::mCherry* (males and females)

(d,d')
:*sqh-5HT2A::mNeonGreen/ChC::RFPt*; (males and females)

(e,e')
;sqh-5HT2B::mCherry/sqh-5HT2B::mCherry;Rab5::GFP/Rab5::GFP (males and females)

(f,f',f'')
5HT2B -/-: ;*sqh-5HT2A::mNeonGreen/ sqh-5HT2A::mNeonGreen; 5HT2B-GAL4/ TM6C,sb* (males and females)

Endo 5HT2B: ;*sqh-5HT2A::mNeonGreen/ sqh-5HT2A::mNeonGreen*;

Extended Data Fig. 10:
Control: ;;ANI-RBD::mNeonGreen,*sqh-sqh*::mCherry/ ANI-RBD::mNeonGreen,*sqh-sqh*::mCherry

Toll 2,6,8 RNAi: ;;ANI-RBD::mNeonGreen,*sqh-sqh*::mCherry/ ANI-RBD::mNeonGreen,*sqh-sqh*::mCherry

Extended Data Fig. 11:
Control: *;67GAL4/+;sqh-sqh::GFP,Lifeact::mCherry/+* (females) crossed with *;67GAL4/ 67GAL4;* (males)
Cirl -/-: *;$Cirl^{KO}$/67GAL4,$Cirl^{KO}$; sqh-sqh::GFP,Lifeact::mCherry/+* (females) crossed with *;67GAL4,$Cirl^{KO}$/67GAL4,$Cirl^{KO}$;* (males)
Cirl-/- 5HT2A++: *;67GAL4,$Cirl^{KO}$/67GAL4,$Cirl^{KO}$; sqh-sqh::GFP,Lifeact::mCherry/UAS-5HT2A* (females) crossed with *; 67GAL4,$Cirl^{KO}$/67GAL4,$Cirl^{KO}$; UAS-5HT2A/UAS-5HT2A* (males)

Constructs and transgenesis:
Endo-mNeonGreen::Dp114RhoGEF: In order to tag Dp114RhoGEF N-terminally with mNeonGreen at its locus, a KO-attP founder line was first generated by CRISPR/Cas9 mediated editing of the gene (editing performed by InDroso, Christine Le Borgne in Rennes). Whole ORF and UTRs were deleted (from 22 bases after the first non-coding exon to 81 bases before the last exon end) and replaced by an attP-LoxP cassette. This "KO-attP founder" line was sent to BestGene Inc and used for PhiC31 mediated transgenesis. A plasmid containing the deleted genomic sequence plus an N-ter mNeonGreen tag was built, resulting in the N-ter tagging of the gene at the locus. Detailed strategies and sequences are available upon request. Flies are homozygous viable.

UBI-mNeonGreen::ANILrbd (ANI-RBD::mNeonGreen): To construct the mNeonGreen-tagged Rho1 GTP sensor, the same strategy was used as for the mEGFP::ANI-RBD Rho sensor (Munjal et al., 2015, ref. 64). mNeonGreen ORF was fused to the C-terminal end of Drosophila anillin (amino acids 748-1239, Genebank ID: AAL39665), which lacks the N-terminal myosin and actin binding domain but retains its Rho1 binding domain. A GGSGGSGGGS flexible linker was inserted between mNeonGreen and anillin. The transgene is expressed under the ubiquitin p63E promoter. For cloning, the mNeonGreen::ANILrbd ORF replaced the stop-CD8GFP ORF in the Ubi-stop-mCD8GFP plasmid obtained from Stepan Belyakin, Russia (GeneBank ID: KC845568).

UASt-5HT2A::Wt and mNeonGreen : ORF corresponding to 5HT2A-RB was amplified (using RE48265 EST clone) and cloned into UASt-attB. Cter mNeonGreen tag was added after a GGSGGGS flexible aa linker.

sqh-5HT2A-mNeonGreen: The ORF corresponding to 5HT2A-RB was amplified (using the RE48265 EST clone) and cloned into the modified sqh promoter (Garcia et al., Current Biol, 2019), replacing the ORF of sqh-mCherry. Cter mNeonGreen tag was added after a GGSGGGS flexible aa linker.

sqh-5HT2B-mCherry: The ORF corresponding to 5HT2B was amplified and cloned into a modified sqh promoter (Garcia et al, Current Biol, 2019), replacing the ORF of sqh-mCherry. The Cter mCherry tag was added after a GGSGGGS flexible aa linker.

All recombinant expression vectors were constructed using in-fusion cloning (Takara Bio), verified by sequencing (Genewiz) and sent to BestGene Incorporate for PhiC31 site-specific mediated transgenesis in both 9736 (2R, 53B2) and attP2 (3L, 68A4). Fully annotated FASTA sequences of all these vectors and detailed cloning strategies are available on request.

RNA interference in embryos:

dsRNA probes: A 544-bp long dsRNA probes against 5HT2B (CG42796) were constructed encompassing ATG (312b before and 229b after). A PCR product containing the sequence of the T7 promoter (TAATACGACTCACTATAGG) followed by 22-24 nucleotides specific for the gene (forward primer: AATGTTTGCCACCAATATCCGTTC; reverse primer: GGGCCCAGTAGTTGTTCGCATC) was gel purified and then used as a template for *in vitro* RNA synthesis with T7 polymerase using HiScribe™ T7 Quick High Yield RNA Synthesis Kit (NEB, E0250). The dsRNA probe was purified using Sure-Clean (Bioline, BIO-37047) and diluted to a final concentration of 5 µM in RNAse-free water prior to injection.

RNAi and Dextran injection in *Drosophila* embryos:

For dsRNA injection experiments, embryos were collected within 1 hour of egg laying, dechorionated in bleach, rinsed and aligned on coverslips coated with heptane glue. Embryos were desiccated for 5-6minutes and covered with Halocarbon 200 oil and injected with RNAse free water or dsRNA (5µM concentration). Post injected embryos were stored at 18ºC prior to imaging.

Dextran 568 (5mg/ml; 10,000MW; Invitrogen), Dextran 488 (5mg/ml; 70,000MW; ThermoFisher) were injected on the perivitelline space at the end of cellularization.

***Drosophila* live imaging:**

Embryos were prepared as previously described (87), stage 6 embryos were collected from flies caged at room temperature (except for overexpression experiments, where flies were caged at 18 ºC to allow sufficient maternal GAL4 deposition). Time lapse images were acquired every 15 seconds for 30-45 minutes, on Nikon dual camera Eclipse Ti inverted spinning disk microscope (distributed by Roper) with a X100/1.4 oil-immersion objective at ~21-22ºC, controlled by the Metamorph software. 11 z-stacks separated by 0.5 µm were acquired starting from the most apical plane. 491-nm and 561-nm lasers were used to excite GFP or mNeonGreen and mCherry fluorophores respectively. Laser powers were measured and kept constant between controls and perturbed experiments. Bright field time-lapse images were acquired using an inverted microscope (Zeiss) and a programmable motorized stage to record multiple positions over time (Mark&Find module from Zeiss), running on AxioVision software (Zeiss). Images were acquired every 1 minute for 3-4 hours.

***Drosophila* image processing and data analysis:**

All image analyses were performed using Fiji freeware. All images were pre-processed with a 0.5 mean filter to smooth the background, followed by an average or maximum projection of the z-stacks (3-11 z-slices spaced by 0.5µm, depending on the experiment). Background subtraction was performed by taking a rolling sphere of 50 pixels (~4µm). For all quantifications of MyoII levels, an additional cytoplasmic signal was subtracted by taking the

mean intensity of the ROI of 10 pixels in diameter inside the cells from the 2D projected images, which excludes the apical signal. Ecad::GFP or Lifeact Cherry or GAP43::mCherry (depending on the experiment) were used to segment the cells. For Rho1 sensor in 5HT2A loss of function and gain of function (Fig. 4b-h) and Rho1/MyoII in Toll triple RNAi knockdown (Extended Data Fig. 10) and Cirl knockout (Extended Data Fig. 13), the Rho1 sensor signal was used to segment the cells. For the 5HT2A and Cirl genetic interaction (Fig. 3e-g), the average projection of the MyoII signal were used for the segmentation as well as tracking the centroid distance to quantify local extension. The resulting skeletons were dilated by 2 pixels on either side of the one-pixel wide cell-cell interface (5 pixels wide), excluding the vertices and used as junctional masks to extract junctional intensities. For the apical signal quantification, the individual cell masks were shrank by 4 pixels to exclude the junctional signal using the macro by G.Kale (51). Junctional and medial Rho1 or MyoII values were mean intensities calculated from the above masks. All the data points obtained were plotted using GraphPad Prism 9 software.

To quantify the amplitude of polarity, the junctions obtained by the above method were categorized into different orientations, $(0\text{-}15)^{o}$ were considered as transverse junctions (AP junctions) and $(75\text{-}90)^{o}$ as vertical junctions (DV junctions). Mean values of all junctions in the categories were measured and the amplitude of polarity was quantified by taking the ratio of the mean intensity of vertical and transverse junctions.

To quantify the 5HT2A::mNeonGreen membrane signal (Extended Data Fig. 3e,f), the GAP43::mCherry signal was used to segment the cells. For the quantification of the 5HT2B::mCherry signal (Extended Data Fig. 7h,i), the average projection of the 5HT2B::mCherry signal was used for the segmentation. Mask obtained as described above were used to extract the mean values of the signals from the 2D images obtained by average projection of apical z-stacks corresponding to 7 µm. Number of vesicles (in Extended Data Fig. 8f'') were counted manually and normalized with the number of cells (30-60 cells per embryo) counted.
To quantify the co-localization of dextran with 5HT2A::mNeonGreen (Extended Data Fig. 8a') or 5HT2B::mCherry (Extended Data Fig. 8b'), and 5HT2A::mNeonGreen and 5HT2B::mCherry (Extended Data Fig. 8c'), pixel-pixel intensities were correlated using custom-written Python code. To quantify the F-actin levels, Lifeact::mCherry signal were used to segment the cells and mean intensities were measured from the 2D projected images as described above.

Tissue scale dynamics: The extent of elongation in (Extended Data Fig. 1b) was measured by tracking the contact point between the perivitelline membrane and the posterior tissue near the pole cells (marked with pink * in Extended Data Fig. 1a) and normalized to the maximum length the tissue could traverse by measuring the distance between the posterior end of the embryo and the cephalic furrow. Local tissue elongation (Extended Data Fig. 2a,b,i) was measured by tracking (using the manual tracking Fiji plugin) the centroid of cells (on X100 videos, frames acquired every 15 sec, that were two cells apart for 15-20 min after the end of ventral pulling. Relative length was calculated as (L-L0)/L0, where L is the centroid distance between the two tracked cells at each time point and L0 is the initial centroid distance. The tracking data were plotted in Python. T1 events and rosettes were detected using the stable T1 tracker and the rosettes tracker, respectively, included in the ImageJ Tissue Analyzer plugin (B. Aigouy, available at https://grr.gred-clermont.fr/ labmirouse/software/WebPA)74. The tracker automatically detects cells that irreversibly lose contact. Rosettes were detected with the threshold of a minimum distance of 10 pixels. The number of stable T1s or rosettes

obtained at each time point was normalized to the number of cells tracked at that time point (on X60 videos, images acquired every 30 sec or 1 min for 50 min after the cellularization front passed the nucleus) and plotted as cumulative events over 30 min (T0 is the onset of ventral pulling) in custom written Python code.

Scanning fluorescence cross-correlation spectroscopy (sFCCS) in *Drosophila* embryo:
Sample preparation: Embryos were prepared as described above in the *Drosophila* live imaging section. sFCCS measurements were performed during the slow phase of the germ-band extension on late stage 8 or early stage 9 embryos at room temperature ~21-22ºC.

Microscope Setup: Scanning fluorescence cross-correlation spectroscopy (sFCCS) was performed on a Zeiss LSM880 system (Carl Zeiss, Oberkochen, Germany) using a Plan-Apochromat 100x, 1.4NA oil immersion objective. Samples were excited with a 488 nm Argon and a 561 nm diode laser in line interleaved excitation to minimize signal cross-talk. To split excitation and emission light, a 488/561 dichroic mirror was used. Fluorescence was detected between 491 nm and 754 nm on a 32 channel GaAsP array detector operating in photon counting mode. A pinhole of the size of an airy unit was used to reduce out-of-focus light. All measurements were performed at room temperature.

Data acquisition: For sFCCS, a line scan of 128x1 pixels (pixel size 63 nm) was performed perpendicular to the plasma membrane at the cell-cell interface with 403.20 µs scan time. Typically, 100,000 lines were acquired for each excitation line (total scan time ca. 80 s), alternating the two different excitation wavelengths. The effective time resolution is thus 806.4 µs, sufficient to reliably detect the diffusion dynamics observed in the samples described in this work (i.e. diffusion times ~10-100 ms). Laser powers were adjusted to keep photobleaching below 50% at maximum in both channels (average signal decays were ca. 40 % for mNeonGreen and 20 % for mCherry). Typical excitation powers were ca. 8 µW (488 nm) and ca. 12 µW (561 nm). Scanning data were exported as TIFF files, imported and analyzed in MATLAB (The MathWorks, Natick, MA, USA; version R2020a) using custom-written code.

Data analysis: sFCCS analysis was performed as previously described (1,2) with minor modifications. Briefly, all scan lines in each channel were aligned as kymographs and divided into blocks of 2000 lines. In each block, the lines were summed column by column and the lateral position of maximum fluorescence was determined. This position defines the membrane position in each block and was used to align all lines to a common origin. A fit of a function consisting of a Gaussian and a sigmoid component was then fitted to the fluorescence profile in each block. The sigmoid part of the fit was subtracted from all lines in the block, effectively removing background fluorescence. Finally, all aligned and background corrected line scans were temporally averaged over the entire kymograph and fitted with a Gaussian function. The obtained waist of this function was typically in the range of 0.25-0.5 µm, indicating that the corrections for lateral movement and background signal were effective. The pixels corresponding to the PM were defined as pixels within ± 2.5SD of the Gaussian peak. In each line and channel, these pixels were integrated, providing membrane the fluorescence time series $F_i(t)$ in channel *i*. In order to correct for depletion due to photobleaching, a two-component exponential function was fitted to the fluorescence time series for each spectral species, $F_i(t)$, and a correction formula was applied (3,4). Finally, the autocorrelation functions (ACFs; g= green channel, r =red channel) and the cross-correlation function (CCF) were calculated as follows, using a multiple tau algorithm:

$$G_{auto,i}(\tau) = \frac{\langle \delta F_i(t) \delta F_i(t+\tau) \rangle}{\langle F_i(t) \rangle^2},$$

$$G_{cross}(\tau) = \frac{\langle \delta F_g(t) \delta F_r(t+\tau) \rangle}{\langle F_g(t) \rangle \langle F_r(t) \rangle},$$

where $\delta F_i(t) = F_i(t) - \langle F_i(t) \rangle$ and $i = g, r$.

To avoid artefacts caused by long-term instabilities or single bright events, CFs were calculated segment-wise (10 segments) and then averaged. Segments showing clear distortions (typically less than 20% of all segments) were manually removed from the analysis (3).
A model for two-dimensional diffusion in the membrane and Gaussian focal volume geometry

(1) was fitted to all CFs:

$$G(\tau) = \frac{1}{N}\left(1 + \frac{\tau}{\tau_d}\right)^{-1/2}\left(1 + \frac{\tau}{\tau_d S^2}\right)^{-1/2}$$

To ensure convergence of the fit for all samples (i.e. ACFs and CCFs of correlated and un-correlated data), positive initial fit values for the particle number *N* and thus $G(\tau)$ were used. In the case of uncorrelated data, i.e. for CFs fluctuating around zero, this constraint can generate low, but positive correlation amplitudes due to noise. From the diffusion time τ_d, the diffusion coefficient D was determined by $D = \frac{\omega_0^2}{4\tau_d}$. The waist ω_0 was determined from point FCS measurements with Alexa Fluor® 488 (Thermo Fisher Scientific, Waltham, MA, USA) dissolved in water at 20 nM, which were performed at the same laser power and 2µm depth to minimize aberrations. The structure parameter *S* was fixed to the average value determined in calibration measurements, typically around 5. From the determined particle number *N*, the protein surface concentration c was quantified: $c = \frac{N}{A_{\text{eff}}} = \frac{N}{\pi\omega_0^2 S}$, where $A_{\text{eff}} = \pi\omega_0^2 S$ is the effective detection area (1).

Relative cross-correlation values (rel.cc.) were calculated from the amplitudes of the ACFs and

CCFs:

$$rel.cc. = max\left\{\frac{G_{cross}(0)}{G_{auto,g}(0)}, \frac{G_{cross}(0)}{G_{auto,r}(0)}\right\},$$

where $G_{cross}(0)$ is the amplitude of the CCF and $G_{auto,i}(0)$ is the amplitude of the ACF in the *i*-th channel. Whereas a rel.cc. value of 1 is theoretically expected for complete binding in 1:1 stoichiometry, experimentally determined rel.cc. values are usually lower due to limited overlap of the detection volumes of the two channels and non-fluorescent states of the fluorescent proteins used to tag the proteins of interest (5,6). Thus, rel.cc. values obtained in positive control samples (e.g. fluorescent protein hetero-dimer constructs) are typically in the range of 0.4 to 0.7, depending on the choice of fluorophores (5–7).

1. Ries, J. et al. (2006). Biophys. J., 91, 1915–1924

2. Dunsing, V. et al. (2017). Mol. Biol. Cell, 28, 3609–3620

3. Dunsing, V. et al. (2018). J. Vis. Exp., e58582

4. Ries, J. et al. (2009). Biophys. J., 96, 1999–2008

5. Foo, Y.H. et al. (2012). Biophys. J., 102, 1174–83

6. Dunsing, V. et al. (2018). Sci. Rep., 8, 10634

7. Dunsing, V. et al. (2021). Elife, 10,

Chick Experiments:

Chick embryo culture and time-lapse microscopy:

Chick embryos were collected at stage XI and cultured using a modified version of the EC culture system for 5-6h prior to immunofluorescence processing or up to 15h for live imaging experiments. Briefly, embryos were collected using paper filter rings and cultured on a semi-solid albumin/agarose nutrient substrate (mixture of albumin, agarose (0.2%), glucose and NaCl) at 37°C in a humid chamber with or without drugs: DMSO for control embryos and Ritanserin at 20µM, 50µM, 100 µM, and 200µM for treated embryos. For live imaging, embryos collected on filter paper rings were transferred to a bottom glass Petri dish (Mattek inc.) on the same media described above and imaged at 37°C using an inverted microscope (Zeiss Apotome) with a 5X objective.

Chick immunofluorescence:

For antibody staining, chick embryos were fixed in ice-cold 4% formaldehyde/PBS for at least 1 h, permeabilized in PBS/0.1% Triton X-100 (PBT 0.1%), and blocked in PBT 0.1%/10% goat serum (from Gibco). Primary antibodies used in this study were mouse anti-ZO1 (Invitrogen ZO1-1A12) and rabbit anti-pMyosin light chain 2 (Cell Signaling Technology CST-3671S and CST-3674S). Secondary antibodies conjugated to AlexaFluor 488 or 555 were purchased from Jackson ImmunoResearch Laboratories, Inc. and used at 1:500 dilutions. Embryos were then mounted between slide and coverslip using Vectashield (Vector Laboratories) containing DAPI.

Chick image acquisition:

Optical sections of fixed samples were obtained on a confocal microscope (Zeiss LSM 880 or LSM 700) using 20X (Plan Apochromat NA 0.8) objectives and ZEN software (Zeiss). Fiji software was used for image processing and data analysis.

Analysis of tissue flows in chick embryo:

Following a common approach to describe the morphogenesis of epithelial sheets (1), the motion of the planar epiblast was described as a continuous, two-dimensional flow field. Time-lapse movies of embryos were analyzed using custom Java software based on the ImageJ API for image processing (2). Briefly, particle image velocimetry (PIV) was used to evaluate the local displacement of the tissue between successive movie frames. The resulting displacement fields were used to reconstruct cell trajectories.

1. S. J. Streichan, M. F. Lefebvre, N. Noll, E. F. Wieschaus, B. I. Shraiman, Global morphogenetic flow is accurately predicted by the spatial distribution of myosin motors. *eLife* **7**, e27454 (2018). doi:10.7554/eLife.27454 Medline
2. Saadaoui, M., Rocancourt, D., Roussel, J., Corson, F., & Gros, J. (2020). A tensile ring drives tissue flows to shape the gastrulating amniote embryo. *Science (New York, N.Y.)*, *367*(6476), 453–458. https://doi.org/10.1126/science.aaw1965

Statistics and Reproducibility:

Data were pooled from at least 4 to 37 independent experiments. Each embryo was considered an independent experiment. For double-stranded RNA injection experiments (Fig. 5 a-d and f-h), each mount was considered as an independent experiment. All p-values were calculated using a two-tailed Mann-Whitney test in GraphPad Prism 9. Box plots extend from the 25th to the 75th percentile and whiskers are minimum and maximum values. All experiments were repeated at least three times. All genetic crosses with overexpression were repeated at least three times. Chick experiments were performed 2-3 times per condition on 6-12 embryos, each embryo was considered an independent experiment. In all figures, n.s.: $p>0.05$, * $p< 0.05$, ** $p<0.005$, *** $p<0.0005$, **** $p<0.00005$ from Mann-Whitney test. No statistical methods were used to determine sample size. The experiments were not randomized and the investigators were not blinded to allocation during the experiments and outcome assessment.

Video Legends

Video 1:
Bright-field time lapse of 5HT2A and 5HT2B null mutant embryos. WT (top panel), *5HT2A-/-* (middle panel) and *5HT2B-/-* (bottom panel). Images acquired every 1 min. A, Anterior; P, Posterior; D, Dorsal; V, Ventral.

Video 2:
MyoII dynamics in 5HT2A loss of function (*5HT2A-/-*). Live 100X imaging of MyoII (*sqh*::mCherry, left panels) and Ecad::GFP (right panels) in the ectoderm during germ-band extension (GBE). Top panels: Control; Bottom panels: 5HT2A null mutant, *5HT2A-/-*. Video represents maximum projection of apical 10 planes spaced by 0.5 µm acquired every 15 sec.

Video 3:
MyoII dynamics in 5HT2A gain of function (5HT2A++). Live 100X imaging of MyoII (*sqh*::mCherry, left panels) and Ecad::GFP (right panels) in the ectoderm during GBE. Top panels: Control; Bottom panels: 5HT2A over-expression, 5HT2A++. Video represents maximum projection of apical 10 planes spaced by 0.5 µm acquired every 15 sec.

Video 4:
MyoII dynamics in Trh loss of function (Trh^{01}). Live 100X imaging of MyoII (*sqh*::mCherry, left panels) and Ecad::GFP (right panels) in the ectoderm during GBE. Top panels: Control; Bottom panels: Trh null mutant, Trh^{01}. Video represents maximum projection of apical 10 planes spaced by 0.5 µm acquired every 15 sec.

Video 5:
MyoII dynamics in Trh gain of function (Trh++). Live 100X imaging of MyoII (*sqh*::mCherry, left panels) and Ecad::GFP (right panels) in the ectoderm during GBE. Top panels: Control; Bottom panels: Trh over-expression, Trh++. Video represents maximum projection of apical 10 planes spaced by 0.5 µm acquired every 15 sec.

Video 6:
MyoII dynamics in Trh knock-out and 5HT2A over-expression (Trh-/- 5HT2A++). Live 100X imaging of MyoII (*sqh*::mCherry, left panels) and Ecad::GFP (right panels) in the ectoderm during GBE. Top panels: Control; Middle panels: 5HT2A++; Bottom panels: Trh-/- 5HT2A++. Video represents maximum projection of apical 10 planes spaced by 0.5 µm acquired every 15 sec.

Video 7:
MyoII dynamics in 5HT2A knock-out and Trh over-expression (*5HT2A-/-* Trh++). Live 100X imaging of MyoII (*sqh*::mCherry, left panels) and Ecad::GFP (right panels) in the ectoderm during GBE. Top to bottom panels: Control; Trh++; *5HT2A-/-*; *5HT2A-/-*Trh++. Video represents maximum projection of apical 10 planes spaced by 0.5 µm acquired every 15 sec.

Video 8:
MyoII dynamics in Toll triple knock-down following 5HT2A over-expression. Live 100X imaging of MyoII (*sqh*::mCherry, left panels) and Ecad::GFP (right panels) in the ectoderm during GBE. Top to bottom panels: Control; 5HT2A++; Toll-2,6,8RNAi; 5HT2A++ Toll-2,6,8RNAi. Video represents maximum projection of apical 10 planes spaced by 0.5 µm acquired every 15 sec.

Video 9:
MyoII dynamics in Cirl and 5HT2A genetic interaction. Live 100X imaging of MyoII (*sqh*::mCherry) in the ectoderm during GBE. Top to bottom panels: Control; *5HT2A-/-*; *Cirl-/-* ; *Cirl-/- 5HT2A-/+*. Video represents maximum projection of apical 10 planes spaced by 0.5 µm acquired every 15 sec.

Video 10:
F-actin and MyoII dynamics in Cirl knock-out and 5HT2A over-expression. Live 100X imaging of actin (Lifeact::mCherry, left panels) and MyoII (*sqh*::mCherry, right panels) in the ectoderm during GBE. Top panels: Control; Middle panels: *Cirl-/-*; Bottom panels: *Cirl-/-* 5HT2A++. Video represents maximum projection of apical 10 planes spaced by 0.5 µm acquired every 15 sec.

Video 11:
Rho1-GTP biosensor dynamics in 5HT2A loss of function (*5HT2A-/-*). Live 100X imaging of Rho1 biosensor (ANI-RBD::mEGFP) in the ectoderm during GBE. Top panels: Control; Bottom panels: *5HT2A-/-*. Video represents maximum projection of apical 10 planes spaced by 0.5 µm acquired every 1 min.

Video 12:
Rho1-GTP biosensor dynamics in 5HT2A gain of function (5HT2A++). Live 100X imaging of Rho1 biosensor (ANI-RBD::mEGFP) in the ectoderm during GBE. Top panels: Control; Bottom panels: 5HT2A++. Video represents maximum projection of apical 10 planes spaced by 0.5 µm acquired every 1 min.

Video 13:
Myosin phosphatase dynamics following 5HT2A++. Live 100X imaging of myosin phosphatase (MBS::GFP) in the ectoderm during GBE. Top panels: Control; Bottom panels: 5HT2A++. Video represents maximum projection of apical 10 planes spaced by 0.5 µm acquired every 15 sec.

Video 14:
MyoII dynamics in 5HT2B loss of function (*5HT2B-/-*). Live 100X imaging of MyoII (*sqh*::mCherry, left panels) and Ecad::GFP (right panels) in the ectoderm during GBE. Top panels: Control; Bottom panels: 5HT2B null mutant, *5HT2B-/-*. Video represents maximum projection of apical 10 planes spaced by 0.5 µm acquired every 15 sec.

Video 15:
MyoII dynamics in 5HT2B knock-down. Live 100X imaging of MyoII (*sqh*::mCherry, left panels) and Ecad::GFP (right panels) in the ectoderm during GBE. Top panels: Control; Bottom panels: 5HT2B dsRNA. Video represents maximum projection of apical 10 planes spaced by 0.5 µm acquired every 15 sec.

Video 16:
MyoII dynamics in 5HT2A and 5HT2B double knock-down. Live 100X imaging of MyoII (*sqh*::mCherry, left panels) and Ecad::GFP (right panels) in the ectoderm during GBE. Top to

bottom panels: Control; 5HT2B dsRNA; *5HT2A-/-*; *5HT2A-/-* 5HT2BdsRNA. Video represents maximum projection of apical 10 planes spaced by 0.5 µm acquired every 15 sec.

Video 17:
Rho1 biosensor and MyoII dynamics following Toll-2,6,8 triple knock-down. Live 100X imaging of MyoII (*sqh*::mCherry, left panels) and Rho1 biosensor (ANI-RBD::mNeonGreen) in the ectoderm during GBE. Top panels: Control; Bottom panels: Toll-2,6,8 RNAi. Video represents maximum projection of apical 10 planes spaced by 0.5 µm acquired every 1min.

Video 18:
Brightfield time lapse of chick embryo treated with DMSO; Control (left panel) and Ritanserin 200 µM (right panel). Images acquired every 6 min.

Video 19:
Particle Image Velocimetry (PIV) time lapse of the chick embryo in movie 18. Left panel: Control (DMSO) and right panel: Ritanserin 200 µM. PIV analysis on consecutive images acquired every 6 min.